

Strike-slip Seismicity at the Andaman-Sumatra Subduction Zone: role of the fracture zones and age of the subducting lithosphere

Jensen Jacob^{1*}, Jérôme Dymont², Dibakar Ghosal³, Pawan Dewangan¹

¹CSIR-National Institute of Oceanography, Dona Paula, Goa-403004, India

²Université de Paris, Institut de physique du globe de Paris et CNRS, Paris, France.

³Indian Institute of Technology Kanpur, Kanpur-208016, U.P., India

*Corresponding author Dr. Jensen Jacob

Email: jacob@nio.org; jensensaviojacob@gmail.com

Research Highlights:

- Density, thickness, and “subductability” of the subducting Wharton Basin lithosphere are derived from the lithospheric age.
- Subductability represents the easiness of the lithosphere to subduct at the Andaman-Sumatra Subduction Zone.
- A prominent strike-slip earthquake cluster is observed along the Fracture zone B-C separating lithospheric compartments of high subductability contrast.
- Despite the high subductability contrast between Compartments G-H, slab tearing on the subducting Investigator Fracture Zone prevents strike-slip earthquake generation.

Abstract

A better comprehension of the shallow strike-slip seismicity along the Sunda Trench is achieved by superimposing the Wharton basin fracture zones, magnetic isochrones, and focal mechanisms to the geometry of the subducting plate. The shallow strike-slip seismicity is generally associated with the north-south trending fracture zones of the basins, which segment the subducting lithosphere into eight main compartments named A-H. Strike-slip earthquakes with magnitudes higher than 4.5 Mw in the time period of 2004-2019 are examined with respect to the thickness and density of the subducting lithosphere, estimated from the lithospheric age. Bulk density ranges from ~ 3259 to ~3273 and lithospheric thickness from ~74 to ~100 km between the younger fossil spreading axis and the older Compartment H, respectively. ‘Subductability’, a parameter calculated from lithospheric thickness and bulk density, is coined to represent the easiness of subduction and varies for each spreading compartment depending on the lithospheric age. We propose the correlation between the shallow strike-slip seismicity and the contrasts of lithospheric thickness, density and subductability. Considering the available seismic records from the past four decades, a prominent cluster of strike-slip earthquakes is observed along Fracture Zone B-C, which displays a strong subductability contrast, whereas other fracture zones displaying only minor seismicity correspond to low subductability contrasts. Despite a high subductability contrast, slab tearing on the subducting Investigator Fracture Zone between Compartments G-H prevents the generation of strike-slip earthquakes. This result emphasizes the importance of physical and mechanical properties of the subducting lithosphere in localizing the seismicity at subduction zones.

Keywords: Andaman-Sumatra Subduction Zone, Lithospheric age, Subductability, Fracture zones, Strike-slip earthquakes.

1. Introduction

The Indian ocean have been undergoing severe deformation due to the India-Eurasia collision subjected to the changes in the boundary conditions from continental collision to oceanic subduction (Stein and Okal, 1978; Wiens et al., 1985; Royer and Gordon, 1997; Gordon et al., 1998; DeMets et al., 2005), resulting high rate of seismicity. The Indian Ocean deformation zone extends from the CIR and the Chagos–Laccadive Ridge in the Western Indian Ocean to the Investigator Fracture Zone in the Eastern Indian Ocean and displays both extensional and compressional regimes (Gordon et al., 1998) (Figure 1). On either side of the Ninety East Ridge (NER), the direction of compression in the diffused zone varies from north-south in the CIB to northwest-southeast in the Wharton Basin (Delescluse and Chamot-Rooke, 2007). The north-south compression at $\sim 75^{\circ}$ E of the CIB develops long-wavelengths (100-300 km), east-west trending basement folds (McAdoo and Sandwell, 1985) and series of shallow thrusts and reverse faults (Bull and Scrutton, 1990). On the other hand, the Wharton basin reports evidence for many northeast-southwest trending folds (Deplus, 2001). The fracture zones of the Wharton Basin have been reactivating as left-lateral strike-slip faults as a result of intraplate deformation since the late Oligocene (~ 20 Ma) (Royer & Gordon, 1997; Deplus et al., 1998).

The prominent strike-slip earthquakes along the NER (Bergman and Solomon, 1985; Abercrombie et al., 2003) and reactivated fracture zones are reported to be associated after the outbreak of 26th December, 2004 and 28th March, 2005 earthquakes (Engdahl et al., 2007; Lin et al., 2009). Carton et al., (2014) reported that a group of aftershocks ruptured the northward extension of fracture zone F6 (the Fracture Zone B-C of this study) which is claimed to be the best-defined reactivated fracture zone in the pre-2012 seismicity. Moreover, few compressional events with NW-SE oriented P-axes are recorded in the Wharton basin and are reported to be intraplate events (Engdahl et al., 2007; Delescluse et al., 2008). Wharton basin experienced the ever-recorded largest intraplate strike-slip earthquake on 11th April, 2012 of Mw 8.6 (McGuire and Beroza, 2012) with a complex rupture mechanics (Meng et al., 2012; Ishii et al., 2013), followed by a numerous moderate sized aftershock and a great aftershock of Mw 8.2 near the Fracture Zone B-C activating several structural trends (Duputel et al., 2012).

However, the reactivation of the fracture zones in the Wharton basin are reported to be mostly associated with the deformation of the subducting oceanic plates (Delescluse et al., 2012; Carton et al., 2014; Singh et al., 2017), but how the physical parameters of the subducting plate have been influencing the reactivation process of the fractures at the subduction zone are never discussed. We therefor analyze the significance of the old fracture zones in generating recent strike-slip seismicity at the Andaman Sumatra Subduction Zone (ASSZ) and we examine the influence of the physical parameters of the subducting Wharton lithosphere, mainly the age, thickness and density, in

reactivating the fracture zones at ASSZ. We propose an additional parameter called ‘Subductability’, a derivative from lithospheric thickness and bulk density, which refers to the easiness of the lithosphere to subduct at the subduction zone. ‘Subductability’ depends on the age of the subducting lithosphere, which is highly variant for each of the fracture zone compartments of the Wharton lithosphere.

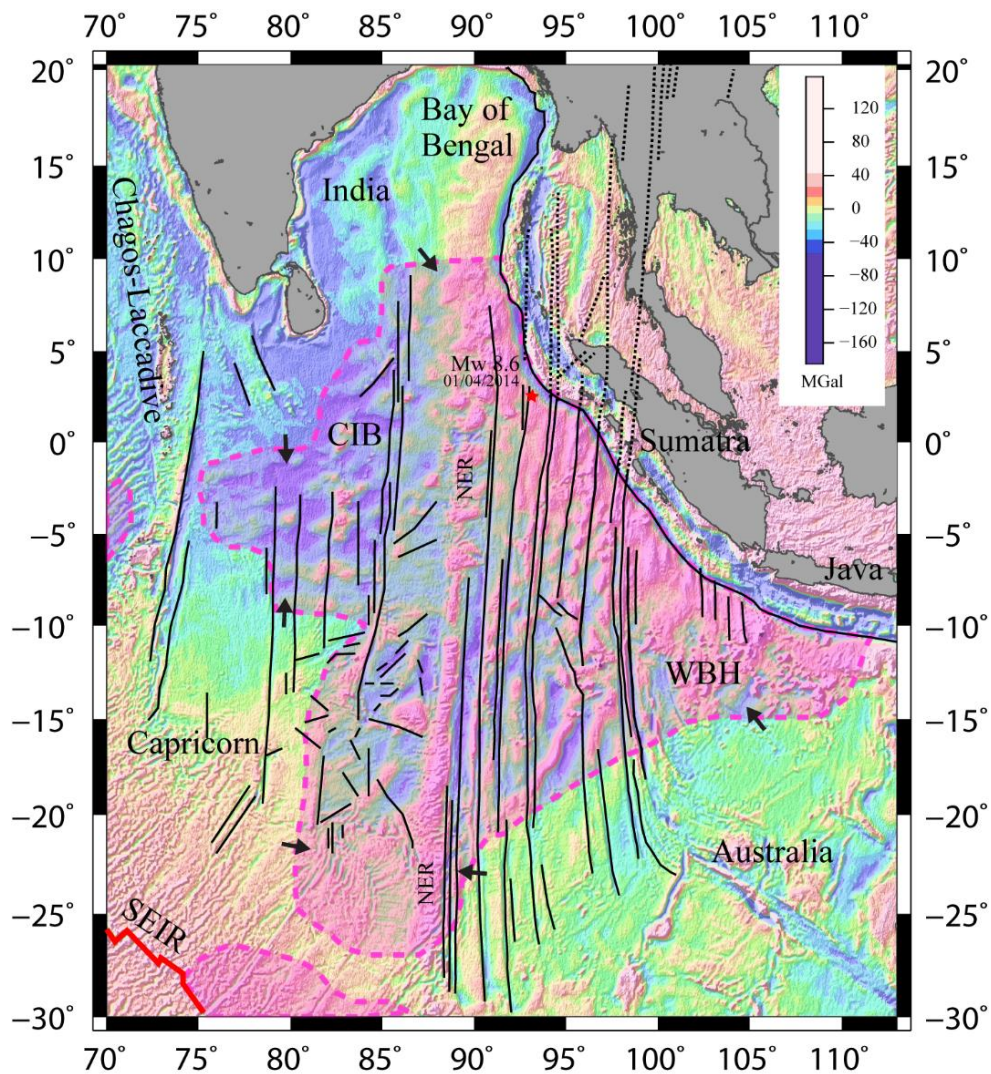


Figure 1: The diffused plate boundary of Indo-Australian plate identified by Royer and Gordon (1997) marked with purple dashed out lines. The deformation zone is shaded in light pink color. The black arrows indicate the direction of the compression within the deformation zone. The Ninety East Ridge (NER) separates the Fracture zones of Central Indian Basin (CIB) (Yatheesh et al., 2019) and the Wharton Basin (WBH) (Jacob et al., 2014) marked in black solid lines. The dashed black lines represent the reconstructed fracture zones of WBH (Jacob et al., 2014). The South East Indian Ridge (SEIR) is marked in red solid line. The red star denotes the epicenter of the 11th April 2012 Mw 8.6 strike-slip earthquake. The background image represents the free air gravity anomaly derived from satellite altimetry (Sandwell et al., 2014).

2. Tectonic set up of the Wharton Basin

The Indo-Australian plate is enclosed by the Southeast Indian ridge and the Wharton Basin in the South. The Himalayan fold-thrust belt forms the northern limit where the Indian plate collides against the Eurasian plate at a rate of 37-44 mm/year (Paul et al., 2001) from west to east. The western limit is bounded by the Central Indian Ridge (CIR), while in the east the lithosphere subducts below the Sumatra subduction setting with a varying rate of ~63-39 mm/year (Prawirodirdjo et al., 2000) from the Java to the Andaman Islands. The Ninety East Ridge (NER), which is a profound north-south oriented linear volcanic ridge, divides the Indian ocean basin into two segments: the Central Indian Basin (CIB) at its west and the Wharton Basin in its east. The spreading in the Wharton basin have ceased since ~40 Ma when the Indian and the Australian plate melded into one plate (Fullerton et al., 1989; Liu et al., 1983) (Figure 1). A series of north-south trending continuous fossil fracture zones dissect the Wharton basin lithosphere into eight compartments, A to H, with varying ages ranging from ~ 83 to ~36 Ma (Jacob et al., 2014). These fracture zones are either simple, double or multiple and the offset between the fossil spreading axis of the fracture zone compartment ranges from ~70 to 900km (Jacob et al., 2014), reflecting the mode of spreading and formation of the oceanic crust at the spreading center.

The fracture zone does not necessarily reactivate to generate strike-slip seismicity, unless influenced by strong intraplate deformation (Lay 2019). The reactivation of the fracture zones in the diffused plate boundary is predominantly oriented in northwest-southeast direction, which is synchronized with the principle horizontal compressional direction of Indo-Eurasian collision (Himalayan uplift) and the northeast-southwest tensional stresses resulted from the slab pull force on the subducting northern Wharton basin at the Sunda Trench due the oblique subduction (e.g., Cloetingh and Wortel, 1985; Coblenz et al., 1998; Delescluse et al., 2012). Before 2004 megathrust earthquake the stress estimated along the fore arc basin of the Andaman and the West Sunda arc show a dominance of compressive stress ($\sim 5.2 \pm 0.65$ mm/year) close to the Nias Island and reduces to the Andaman and Nicaobar Islands region (Radhakrishna and Sanu, 2002). Shamim et al., (2019) reported that the stress field at offshore Simuelue between 1°N and 6°N was significantly altered after the outbreak of 26th December 2004 event and has undergone stress transfer from oblique strike-slip to pure compression. This region again underwent a compressional stress regime after the 2012 twin events. Contrary, the offshore region between 2°N and 2°S experienced pure extension from the time period 2008 to 2015, orienting the extensional axis normal to the trench. However, the convergence rate at the ASSZ is high close to the Java (63 mm/year), showing comparatively lower convergence rate from the Nias Island (50 mm/year) to northwest of the Sumatra (45mm/year) and the lowest convergence rate near the Andaman

accretionary island (39mm/year) (Chlieh et al., 2007, Cattin et al., 2009). Recent bathymetric and reflection seismic data show that compressional stresses in the Wharton Basin are not solely accommodated through the reactivation of fracture zone but also through a complex network of distributed shear zones, thrusts and normal faults (Singh et al., 2017; Hananto et al., 2018).

3. Data and Methods

We have considered the position-corrected Centroid Moment Tensor (CMT) solutions (Dziewonski et al., 1981; Ekström et al., 2012) for shallow strike-slip earthquakes ranging between 0-60 km depth with magnitudes higher than 4.5 Mw recorded between 2004 and 2019. We made a comparison of the data distribution from 1976 (the oldest available earthquakes from the CMT catalogue) to 26th December 2004 megathrust earthquake, between 2004 megathrust and April 11th 2012 earthquakes and finally, 2012 earthquake to 2019. The participation of the fracture zones in earthquake generation is prominently noticed only after 26th December 2004 megathrust earthquake. Hence, we have concentrated on the focal mechanisms after the 2004 megathrust event. Detailed explanation of the criteria for data selection is explained in Figure 2. For better comprehension, the selected focal mechanisms are categorised based on the year of occurrence and plotted on the Free air gravity anomaly background derived from satellite altimetry (Sandwell et al., 2014) (Figure 3) and provided as supplementary material.

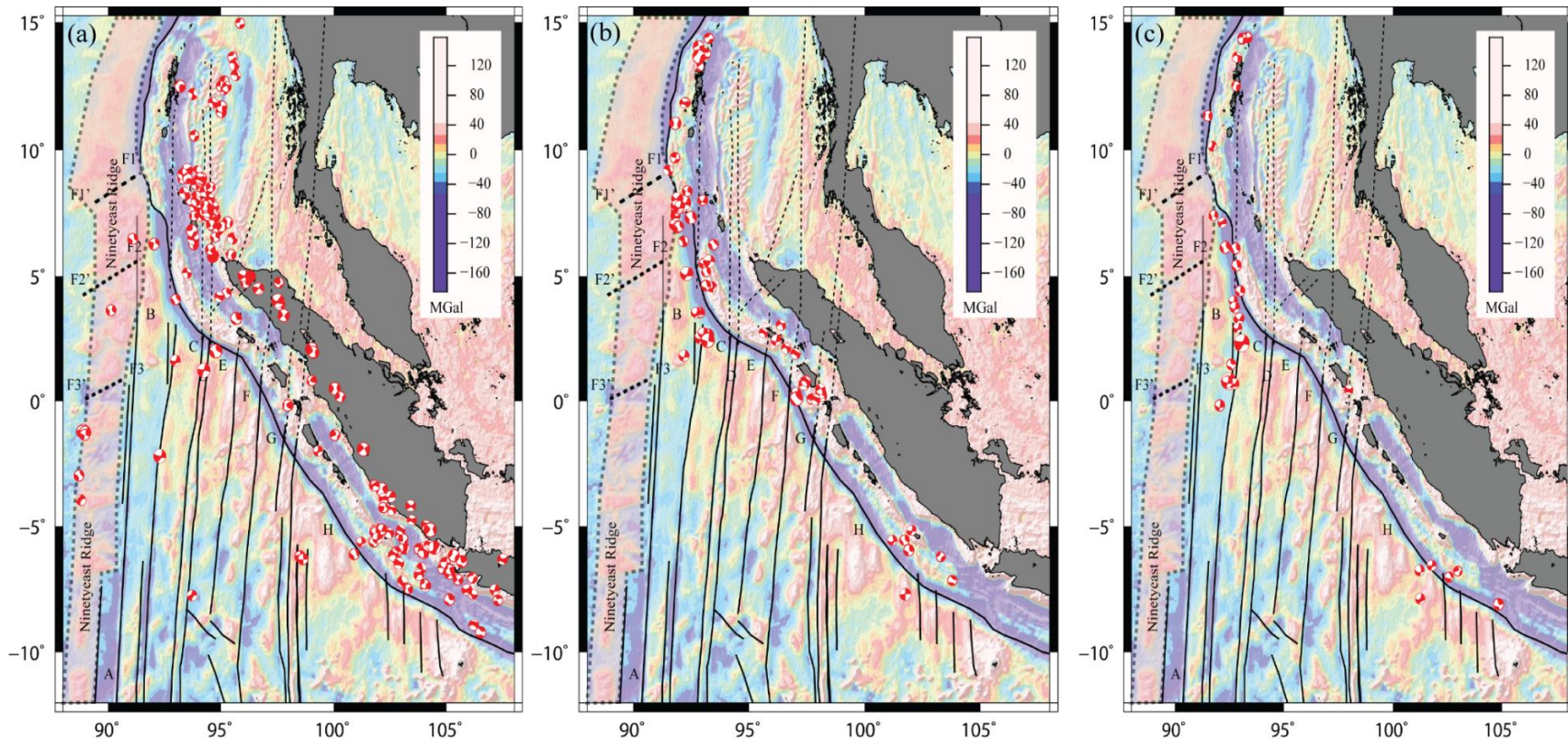


Figure 2: Comparison of strike-slip earthquakes extracted from *Global Centroid Moment Tensor* data base along the ASSZ is performed by categorising the strike-slip focal mechanisms based on their year of occurrence. Focal mechanism for each category is plotted on the background of free air gravity anomaly derived from satellite altimetry (Sandwell et al., 2014). a) represents the distribution of the strike-slip earthquake from 1976 to 26th December 2004 megathrust earthquake which are clustered in three localities mainly the Andaman back arc basin, the south of the Andaman fore arc region and between the southern Sumatran fore arc basin (the Bengkulu basin) and the Java Basin. A prominent clustering of strike-slip earthquakes is evident on the reconstructed Fracture Zones C-D and D-E, close to the Nicobar accretionary island. Inside the Wharton Basin a few strike-slip earthquakes are aligned along the Fracture Zone B-C and C-D and D-E b) represents the location of the strike-slip earthquakes spanning between 26th December 2004 and April 11th 2012 earthquakes. The reactivation of the fracture zone is evident by the high magnitude strike-slip earthquakes along the Fracture Zone B-C c) High magnitude strike-slip earthquakes after the 2012 April Wharton basin earthquakes till 2019 are more concentrated along the Fracture Zone B-C representing the continuous reactivation of fracture zones of the Wharton Basin.

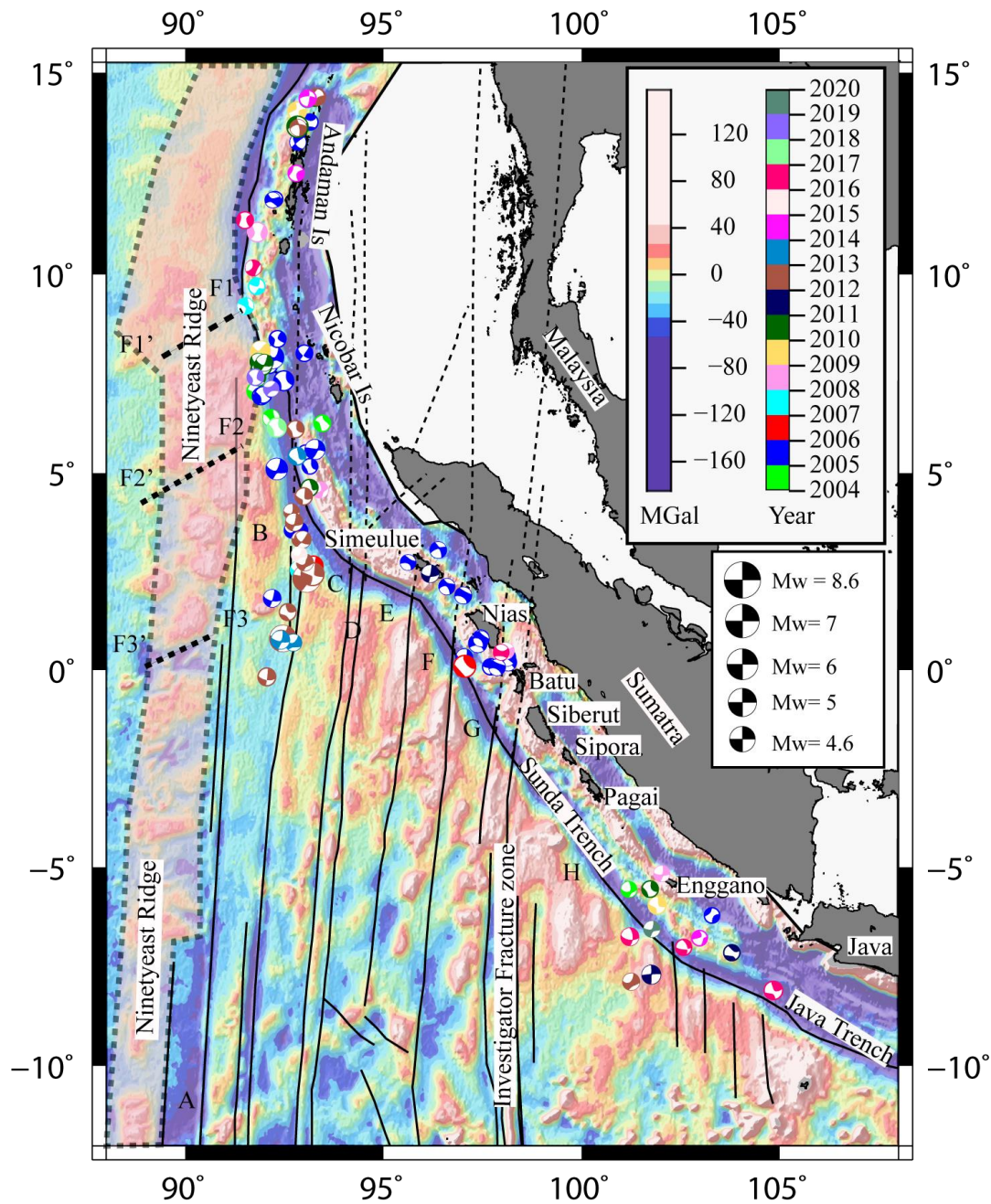


Figure 3: Free air gravity anomaly derived from satellite altimetry (Sandwell et al., 2014) in the Wharton Basin area. Solid black lines represent actual fracture zones and dashed black lines reconstructed fracture zones. Focal mechanisms extracted from *Global Centroid Moment Tensor* data base are plotted for earthquakes with magnitude higher than 4.5 Mw and depth less than 60 km for the time span 2004-2019, with colors indicating their year of occurrence. Thick dashed lines on the Ninety East Ridge represents the location of *en-echelon* faults F1-F1', F2-F2', F3-F3' (after Subrahmanyam et al., 2008).

The isochron interpretation of the Wharton Basin had been validated by two- and three-plate reconstructions involving Australia, Antarctica, and India (Jacob et al, 2014). Using the Euler's plate rotation parameters, the reconstruction of the fracture zones and age of the northern Wharton Basin lithosphere subducted under the Sumatra Trench is proposed. The age grid is overlain by the position-corrected strike-slip CMT solutions along the ASSZ (Figure 4a). The geometry of the subducted lithosphere in the ASSZ has been modeled by the tomography study of Pesicek et al. (2008). The reconstructed fracture zones and magnetic isochrons are superimposed to the geometry of the subducting plate as imaged by seismic tomography to achieve a 3D model of the subducting lithosphere (Jacob et al, 2014). We have updated our previous 3D model by superimposing the strike-slip hypocenters along the subduction zone (Figure 4b). This model (Figure 4a, 4b) provides an interesting means to perform a compartment-wise analysis of the role of fracture zones, both directly identified and reconstructed, in generating strike-slip seismicity in the subduction zone.

We have estimated the thickness of the subducting Wharton lithosphere based on the half-space cooling model by Turcotte and Schubert, 1982. For the lithosphere younger than 70 Ma, the square root of the age \sqrt{t} is directly proportional to the depth of the lithosphere (Parsons and Sclater, 1977; Stein and Stein, 1992) implying a maximum heat flow for the young lithosphere at the ridge axis which progressively lowers with age and distance to the axis. The thickness estimated for lithosphere younger than 70 Ma shows less discrepancy in its heat flow and bathymetry predictions. For the older lithosphere, the plate cooling model imposes a constant basal temperature at a specific depth (McKenzie, 1967; Sclater and Francheteau, 1970; Parsons and McKenzie, 1978), which has been updated to minimize the observed discrepancy between measured and predicted heat flow and bathymetry for the older lithosphere (e. g. Doin and Fleitout, 1996; Korenaga and Korenaga, 2008; Hasterok, 2013). According to Turcotte and Schubert (1982) the thickness of the lithosphere $z_l = 2.32\sqrt{\kappa t}$ where κ is the thermal diffusivity (about $10^{-6} \text{ m}^2\text{s}^{-1}$), t is the age (in s). However, the subducting northern Wharton basin includes both younger ($< 70 \text{ Ma}$) and older ($> 70 \text{ Ma}$) lithosphere. Hence to prevent the over or under estimation of thickness, z_l is weighted by the ratio $\frac{d_p(t) - d_0}{d_h(t) - d_0}$, where $d_p(t)$ and d_0 are the depths at ages t and zero in the plate model GDH1 of Stein and Stein (1992) and $d_h(t)$ the depth at age t in the half-space model approximation of Parsons and Sclater (1977; their equation (21) for ages younger than 70 Ma). As expected, this ratio is close to 0.95 at 70 Ma and decreases to 0.7 at 160 Ma. We

use the lithospheric thickness to derive the “subductability” of the down going plate, which gives a representation of how easily the lithosphere may enter subduction for each of the Wharton Basin compartments. Subductability is defined as the net pressure applied on the asthenosphere by the subducting lithosphere, given by $S = g (\rho_l - \rho_a) z_l$ where ρ_l is the bulk lithosphere density, ρ_a the bulk asthenospheric mantle density (3250 kg m^{-3}), and g the acceleration of the gravity ($\sim 9.81 \text{ ms}^{-2}$). Subduction happens when ρ_l exceeds ρ_a . A low subductability indicates a higher resistance offered by the hot asthenosphere to the subducting plate (Jacob et al, 2014).. The bulk density (ρ_l) of the lithosphere is estimated from the lithospheric thickness. The bulk density (ρ_l) of the lithosphere combines a mean density of 2860 kg m^{-3} (Carlson and Herrick, 1990) for the $\sim 7 \text{ km}$ thick crust (z_c) formed at spreading ridge (White et al., 1992) and a mean density of 3300 kg m^{-3} for the underlying lithospheric mantle of varying thickness (z_m) that directly depends on the age of the lithosphere (Stern, 2002), hence $\rho_l = ((2860 \times z_c) + (3300 \times z_m))$.

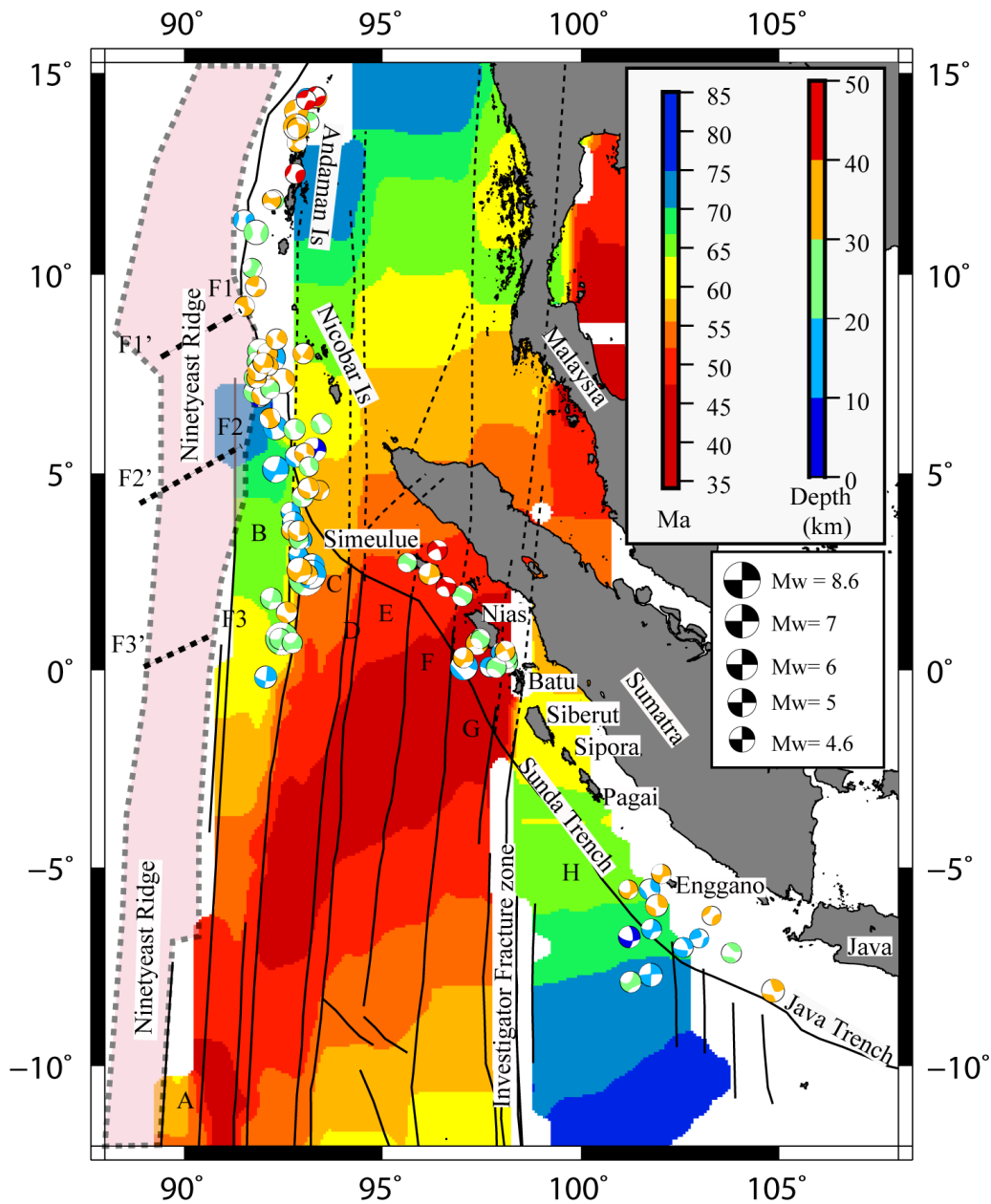


Figure 4a: Age of the oceanic lithosphere in the Wharton Basin showing Compartments A to H. Solid black lines represent actual fracture zones and dashed black lines reconstructed fracture zones. Focal mechanisms extracted from *Global Centroid Moment Tensor* data base are plotted for earthquakes with magnitude higher than 4.5 Mw and depth less than 60 Km for the time span 2004-2019, with colors indicating their depth. Thick dashed lines on the Ninety East Ridge represents the location of *en-echelon* faults F1-F1', F2-F2', F3-F3' (after Subrahmanyam et al., 2008).

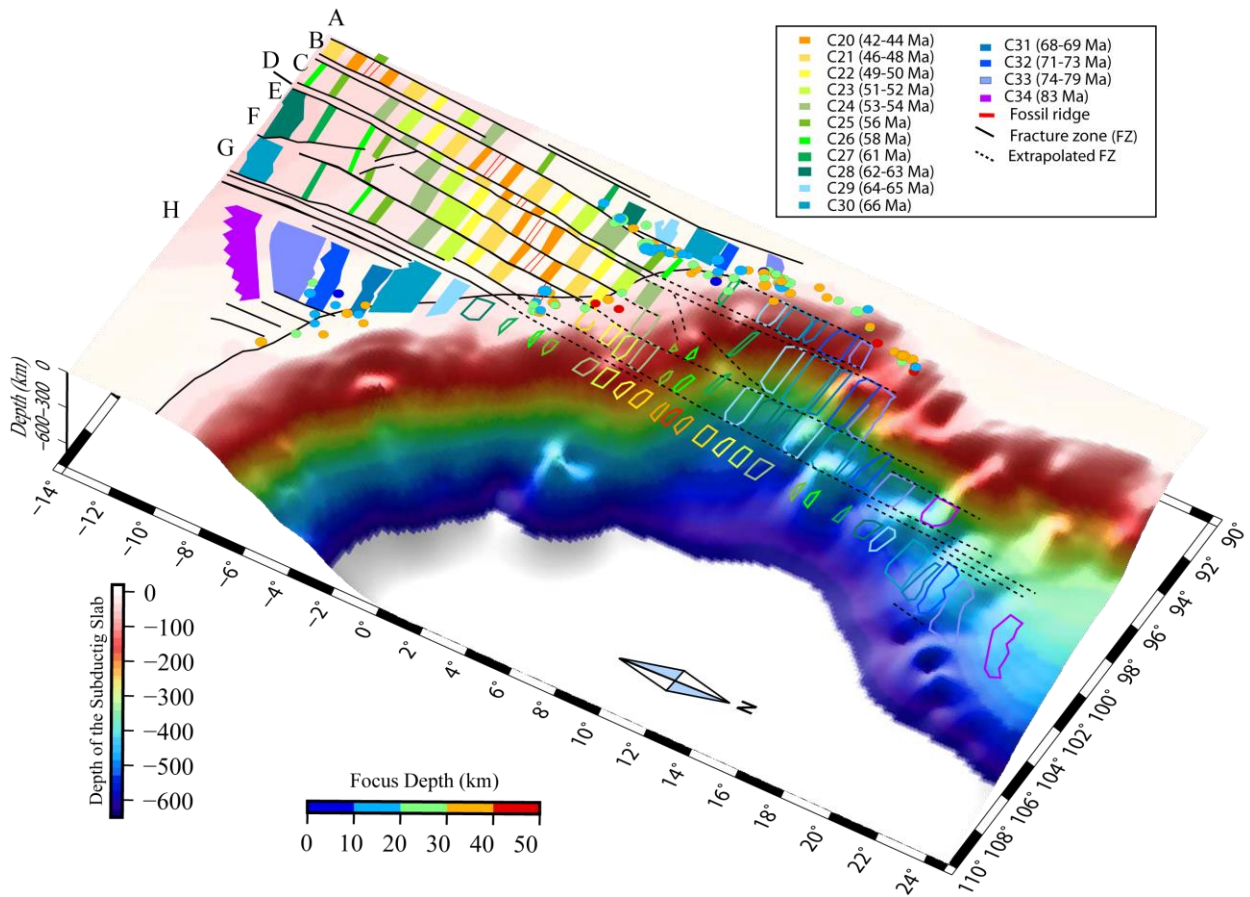


Figure 4b: Three-dimensional view of the subducting lithosphere in the Andaman-Sumatra subduction zone. Solid black lines represent actual fracture zones and dashed black lines reconstructed fracture zones. Normally magnetized blocks are displayed in filled colored boxes for the identified isochrons and hollow colored boxes for reconstructed isochrons. Colored circles show the strike-slip earthquake epicenters considered for this study, with colors indicating their depth.

4. Results

4.1 Distribution of strike-slip seismicity

We have considered strike-slip earthquakes of less than 60 km depth distributed along the ASSZ between Andaman Islands in northwest and Enggano Island in southeast. Along the subduction zone the distribution of strike-slip earthquakes varies for each spreading compartment (Figure 3). Compartment B has the largest cluster of strike-slip earthquakes within a depth range of 10 to 40 km. The single fracture zone which separates Compartments B and C splits to a double fracture

zone at $\sim 1^\circ\text{N}$ forming a short, intermediate, knife-edge segment from $1\text{-}5^\circ\text{N}$. Strike-slip earthquakes seem to cluster on the bifurcation zone. They extend southward up to 1°S and can be traced northward to the trench near Andaman and Nicobar Islands. The strike-slip earthquakes concentrated on Andaman Islands have deeper epicenters reaching 50 km. Within the time span of 2004-2019, no strike-slip earthquake is observed on the fracture zones separating Compartments C-D, D-E and E-F. A small cluster of low magnitude earthquakes lie between 20 and 50 km beneath Simeulue Island, in which the shallower ones (20-30 km) are aligned parallel to the trench on both sides of the reconstructed fracture zone separating Compartments E and F. Many strike-slip earthquakes are observed in Compartment G, near Nias Island, where the Wharton Basin fossil spreading center enters the subduction zone. The depth of these earthquakes ranges from 10 to 40 km. They do align neither along the fracture zones nor parallel to the trench but instead along the east-west trend of the fossil spreading center. The older lithosphere from the eastern end of the Compartment H, bounded by several fracture zones constrained by the free-air gravity anomaly derived from satellite altimetry (Figure 3), exhibits scattered strike-slip earthquakes within the depth range of 10 to 40 km. Conversely, the multiple Investigator Fracture Zone separating Compartments G and H does not show any strike-slip earthquakes, despite a subductability contrast similar to that observed between Compartments B and C.

A large cluster of strike-slip earthquake is observed where the northern end of Compartment B interacts with the subduction zone. To the west, Compartment B directly abuts the NER north of 6°S , whereas further south it is bounded by the narrow Compartment A with a maximum age of ~ 60 Ma (Figures 4a). The NER does not form by normal seafloor spreading, so the estimation of age, density, thickness and subductability is impossible by the method we apply. Alternatively, the clustering of strike-slip seismicity at ASSZ due to interaction with the NER is discussed in section 5.1, correlating the trench morphology with tectonic features of the NER. Beyond $\sim 8^\circ\text{N}$ strike-slip clustering deviates from the trench, concentrating more on the accretionary Andaman Islands. The northern extent of the NER, possibly buried under the Bengal Fan sediments (Moeremans and Singh, 2014; Singh and Moeremans, 2017), is uncertain and its interaction with the trench to form the Andaman accretionary islands require more analysis.

4.2 Thickness and Bulk density of the Wharton Basin Lithosphere

Maps of the lithospheric thickness (Figure 5) and density (Figure 6) show significant variations of these parameters along the subduction zone. The lithosphere bounding the NER to the east in Compartment B, ~79 Ma old, has an estimated bulk density of ~3272 and a thickness of ~110 km. In the adjacent Compartment C with younger lithosphere, ~58 Ma old, the density is ~3267 and the thickness ~94 km. The youngest lithosphere of Compartment G contains the fossil spreading ridge, ~36 Ma old, with the lowest density and thickness of ~3259 and ~74 km, respectively. Lithosphere of the wide Compartment H meet the subduction zone with a variety of ages ranging between ~64 Ma immediately east of the Investigator Fracture Zone, for density and thickness of ~3269 and ~100 km, respectively, and ~68 Ma on the eastern side of Compartment H, for density and thickness of ~3270 and ~102 km, respectively. Density of ~3266, ~3266 and ~3264 and thickness of ~90 km, ~89 km and ~87 km is estimated for the younger subducting lithosphere of Compartments D, E and F, respectively aged ~53, ~52 and ~49 Ma. Thickness and bulk density estimated for magnetic chrons from 17 young to 34 young is listed in Table 1

4.3 'Subductability' of the Wharton Basin Lithosphere

Subductability estimated for Compartment B is $\sim 2.37 \times 10^9 \text{ Nm}^{-2}$ where the ~79 Ma-old lithosphere enters the subduction zone, whereas in Compartment C it amounts for $\sim 1.59 \times 10^9 \text{ Nm}^{-2}$ for ~58 Ma old lithosphere. The large offset of Fracture Zone B-C results in an important age difference (21 Ma) between the older lithosphere of Compartment B with the adjacent younger one of Compartment C, which in turns converts to a large contrast ($\sim 0.778 \times 10^9 \text{ Nm}^{-2}$) of subductability. The narrow Compartment D presents a subductability of $\sim 1.41 \times 10^9 \text{ Nm}^{-2}$, and the adjacent Compartments E and F a subductability of ~ 1.37 and $\sim 1.22 \times 10^9 \text{ Nm}^{-2}$, respectively. Compartments C, D, E, and F show comparatively younger ages of the lithosphere entering subduction, respectively ~58 Ma, ~53 Ma, ~52 Ma and ~49 Ma, with only small variations resulting in consistently small subductability contrasts between adjacent compartments (at most $0.1 \times 10^9 \text{ Nm}^{-2}$). Compartment G, where the fossil spreading axis enters subduction, displays the youngest lithosphere at the trench with the lower subductability of $\sim 0.65 \times 10^9 \text{ Nm}^{-2}$. The lithosphere entering the subduction zone in Compartment H extends through the older magnetic Chrons 29, 30 and 31 of age ~64 - ~68 Ma with subductability ranging between ~ 1.86 and $\sim 2.01 \times 10^9 \text{ Nm}^{-2}$ (Figure 7). Compartment G presents a large contrast of subductability ($\sim 0.58 \times 10^9$

Nm⁻²) with Compartment F and an even larger one ($\sim 1.2 \times 10^9$ Nm⁻²) with Compartment H. Subductability estimated for magnetic chrons from 17 young to 34 young is listed Table 1

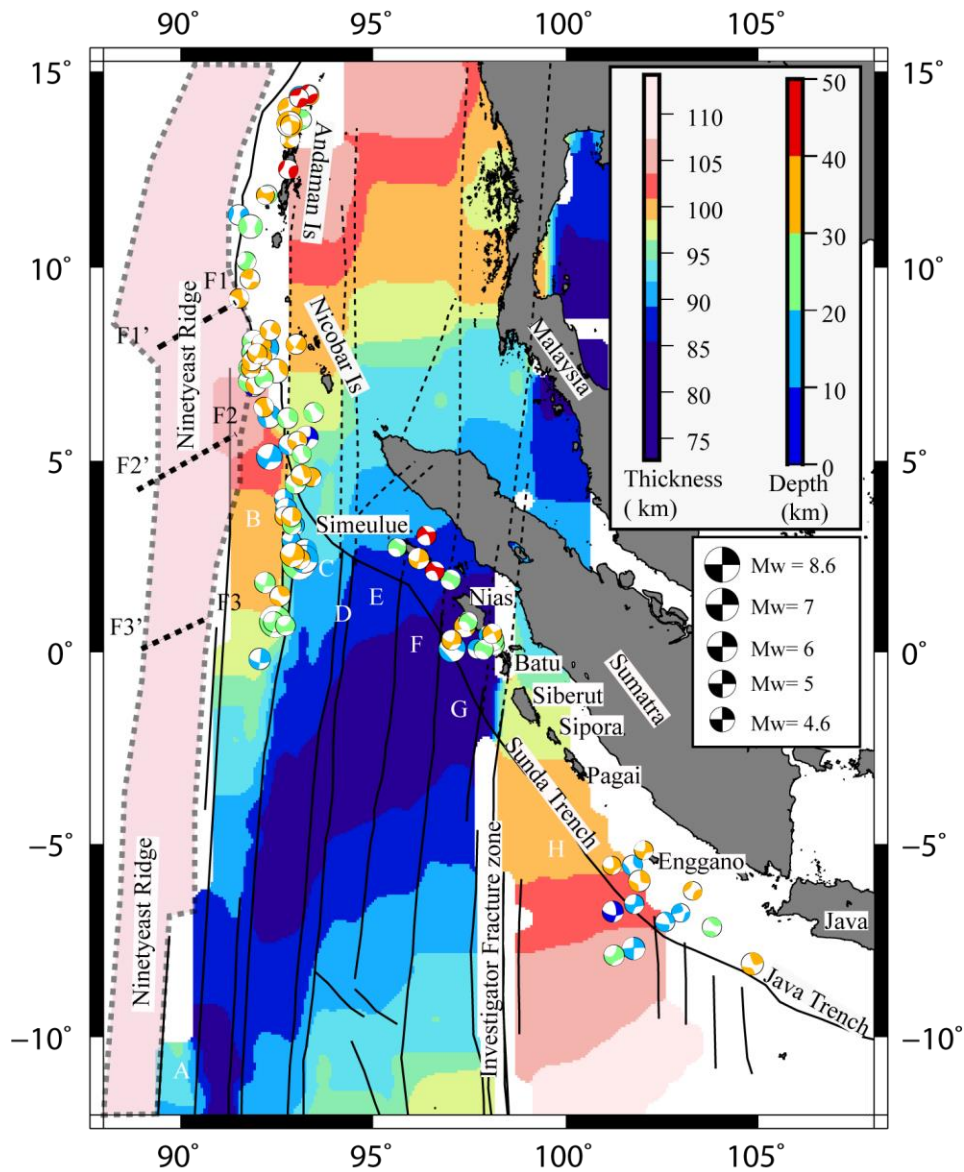


Figure 5: Lithospheric thickness of the Wharton Basin and its reconstructed part. Solid black lines represent actual fracture zones and dashed black lines reconstructed fracture zones. Focal mechanisms extracted from *Global Centroid Moment Tensor* data base are plotted for earthquakes with magnitude higher than 4.5 Mw and depth less than 60 Km for the time span 2004-2019, with colors indicating their depth. Thick dashed lines on the Ninety East Ridge represents the location of *en-echelon* faults F1-F1', F2-F2', F3-F3' (after Subrahmanyam et al., 2008).

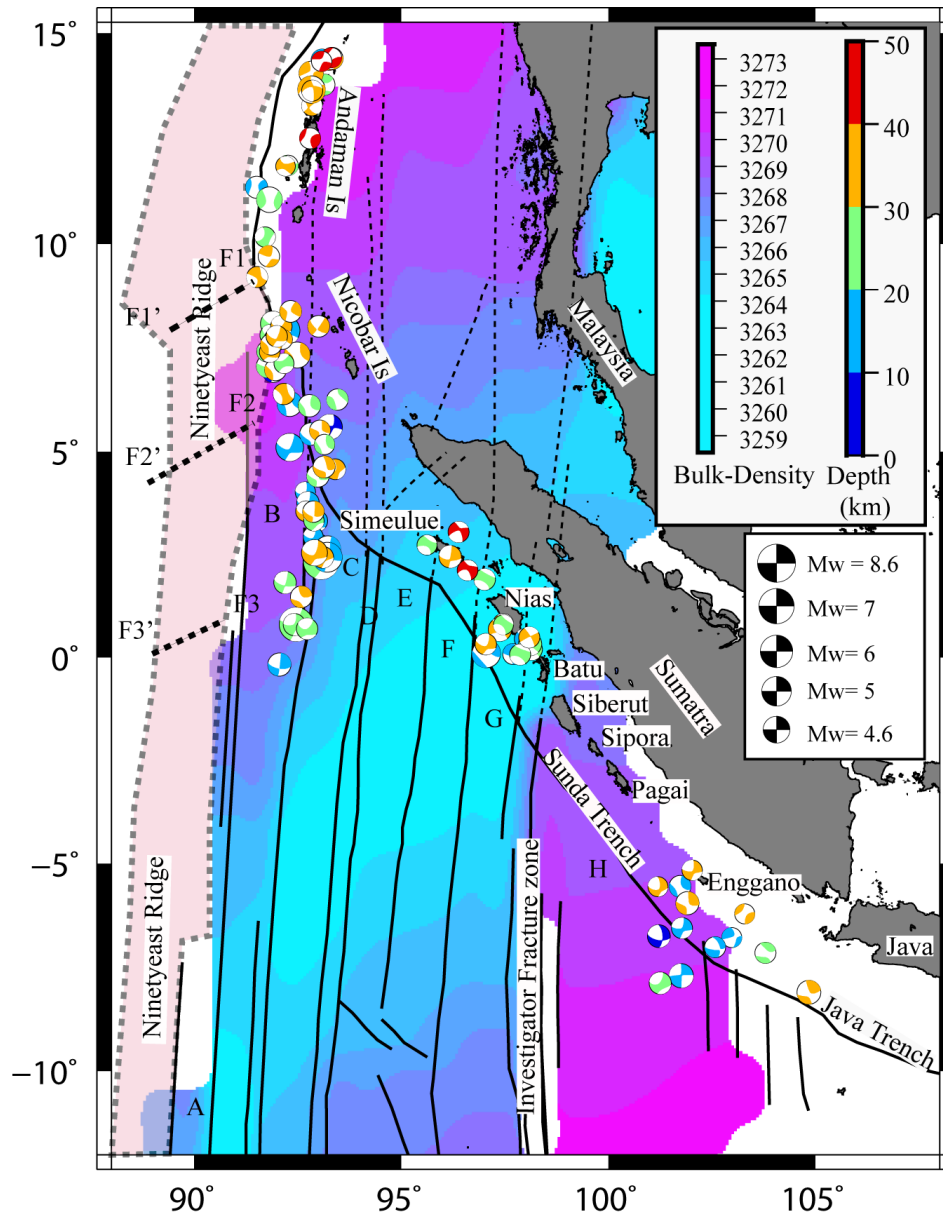


Figure 6-: Bulk lithospheric density of the Wharton Basin and its reconstructed part. Solid black lines represent actual fracture zones and dashed black lines reconstructed fracture zones. Focal mechanisms extracted from *Global Centroid Moment Tensor* data base are plotted for earthquakes with magnitude higher than 4.5 Mw and depth less than 60 Km for the time span 2004-2019, with colors indicating their depth. Thick dashed lines on the Ninety East Ridge represents the location of *en-echelon* faults F1-F1', F2-F2', F3-F3' (after Subrahmanyam et al., 2008).

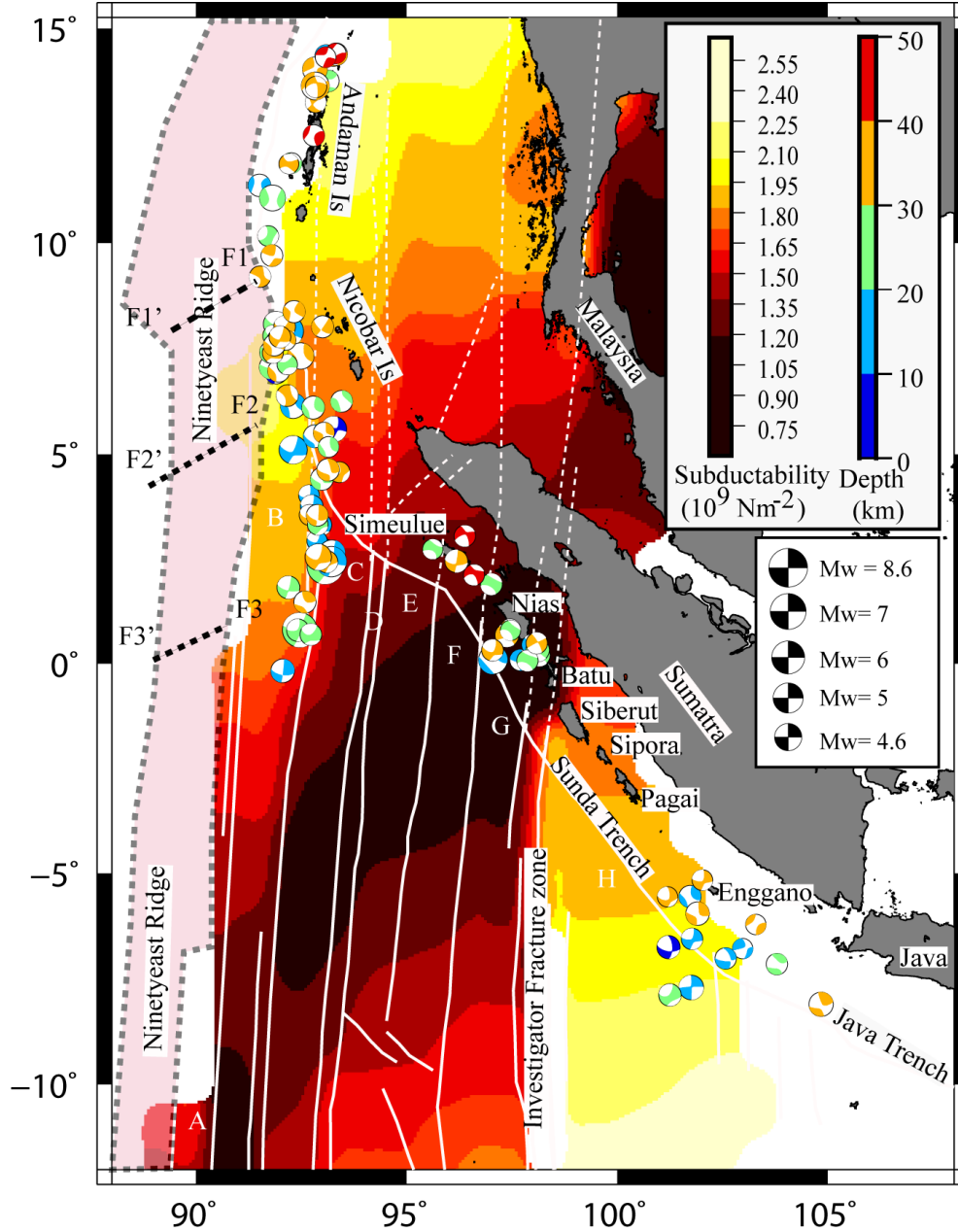


Figure 7: Lithospheric ‘subductability’ of the Wharton Basin and its reconstructed part. Solid white lines represent actual fracture zones and dashed white lines reconstructed fracture zones. Focal mechanisms extracted from *Global Centroid Moment Tensor* data base are plotted for earthquakes with magnitude higher than 4.5 Mw and depth less than 60 Km for the time span 2004-2019, with colors indicating their depth. Thick dashed lines on the Ninety East Ridge represents the location of *en-echelon* faults F1-F1’, F2-F2’, F3-F3’ (after Subrahmanyam et al., 2008).

Magnetic Chrons	Age (Ma)	Thickness (km)	Bulk-Density	Subductability (10^9Nm^2)
17y	36.618	74.8966174	3258.876647	0.652199083
20y	42.536	80.72224232	3261.844469	0.937945986
20o	43.789	81.90254695	3262.394332	0.995839928
21y	46.254	84.17624368	3263.410104	1.107364752
21o	47.907	85.66716234	3264.046901	1.180494313
22y	49.037	86.67160523	3264.463563	1.229762236
22o	49.714	87.26784421	3264.706359	1.259007758
23y	50.778	88.1967718	3265.078087	1.304571657
23o	51.743	89.03088617	3265.405264	1.345484967
24y	52.364	89.56355031	3265.61101	1.371612143
24o	53.347	90.40030474	3265.929318	1.412654947
25y	55.904	92.54145752	3266.71762	1.517678491
25o	56.391	92.94366456	3266.861647	1.537406746
26y	57.554	93.89720173	3267.198171	1.584177745
26o	57.911	94.18796762	3267.299432	1.598439812
27y	60.92	96.60394033	3268.117243	1.716943273
27o	61.276	96.88579281	3268.209993	1.730768137
28y	62.499	97.84788166	3268.522568	1.777958596
28o	63.634	98.73235713	3268.804553	1.821342117
29y	63.976	98.9973194	3268.888046	1.834338517
29o	64.745	99.59052258	3269.073362	1.863435133
30y	65.578	100.2291339	3269.270412	1.894759016
30o	67.61	101.7701376	3269.735719	1.970345248
31y	67.735	101.8641724	3269.763658	1.974957656
31o	68.737	102.6148419	3269.984849	2.011777996
32y	71.071	104.3424685	3270.481818	2.096518078
32o	73.004	105.7519105	3270.875231	2.165651208
33y	73.619	106.1964137	3270.997137	2.187454091
33o	79.075	110.0612634	3272.015586	2.377024972
34y	83	112.7597073	3272.685279	2.509383643

Table 1: Thickness, bulk-density and subductability estimated for the subducting northern Wharton lithosphere at the Sunda trench. Age of the magnetic chrons according to the Geomagnetic Polarity Timescales of Cande and Kent (1995). The letters 'y' and 'o' are acronyms for 'younger' and 'older' chron respectively.

5. Discussion

5.1 Ninety East Ridge and Fracture Zone A-B

Like most aseismic ridges, the NER presents a thicker lithosphere (Subrahmanyam et al., 2008; Mukhopadhyay and Krishna, 1995) of volcanic origin different from the conventional basaltic lithosphere formed at the spreading ridges, which makes a practical difficulty in subductability estimation. However, the lower subductability of the NER at ASSZ, than the surrounding oceanic lithosphere is evidenced as low slip and slow rupture speed in the Andaman region during 2004 megathrust earthquake (Gahalaut et al., 2010). The lower subduction rate of ~ 39 mm/year close to the Andaman accretionary island (Chlieh et al., 2007, Cattin et al., 2009) supports the lower subductability of the NER. The shallower depths of the earthquakes (20 to 40 km) suggest the subduction of northern NER at lower depths. The seismic images of the eastern flank of the NER approaching ASSZ shows high amplitude reflections at ~ 60 km underneath the accretionary prisms of the Andaman fore-arc, suggesting the reflectors represents the top of the subducting plate (Moeremans and Singh, 2014).

The morphological expressions of the resistance induced by the lower subductability of NER along ASSZ may include the indentation of the trench observed at 8° N and the fragmentation of the northern NER, creating *en echelon* faults cutting across the northern tip of the NER from latitude $\sim 0^\circ$ and 8° N (F1-F1', F2-F2' and F3-F3' on Figure 8 after Petroy and Wiens, 1989; Subrahmanyam et al., 2008). However, the lower slab pull due to the lower subductability cannot be the sole reason for the *en echelon* faults on NER. As suggested by Petroy and Wiens, 1989, the strike-slip focal mechanisms on the NER is enhanced by the effect of compressional deformation in the Wharton basin and the CIB. The focal mechanisms from the deformation zone show higher horizontal compression perpendicular to the linear gravity highs of the NER (Petroy and Wiens, 1989). A set of ten transverse tear faults (T1-T10) between 6° - 15° N and longitude 90° - 98° E, across the Sunda-Andaman arc is identified by Dasgupta et al. 2003 and Mukhopadhyay et al. 2009 (Figure 8). The predominantly left lateral strike-slip faults show northwest-southeast trend in the north (T1-T4), east-west in the center (T5, T6) and northeast-southwest trend in the south (T7-T10). Apparently, the southern tear faults have a similar trend with the *en echelon* faults trend of the NER (Figure 8). The tear faults are dated pre-2004 and associates its origin with the compressional force due to the

oblique subduction of the NER at the Sunda trench (Dasgupta et al. 2003; Mukhopadhyay et al. 2009).

The strike slip earthquakes clustered at $\sim 7^\circ$ N along ASSZ indicates the possible interaction of the Fracture Zone A-B (which bounds the NER to the East) with the Sunda trench. A set of four of tensional/trans-tensional strike-slip fault systems (TF1, TF2, TF3 and TF4) along the Sunda-Andaman arc shows a northwest-southeast trend in the north (TF1) and east-west trend in the center (TF2) and south (TF3 and TF4) (Mukhopadhyay et al. 2016) (Figure 8). The rupture along TF1, TF3 and TF4 are reported to be induced by 2004 megathrust earthquake, while TF2 is associated with the slab detachment prior to 2004 earthquake (Mukhopadhyay et al. 2016). Though, both the Fracture zone A-B and the trans-tensional faults show a general north-south trend, their mutual association requires more detail analysis.

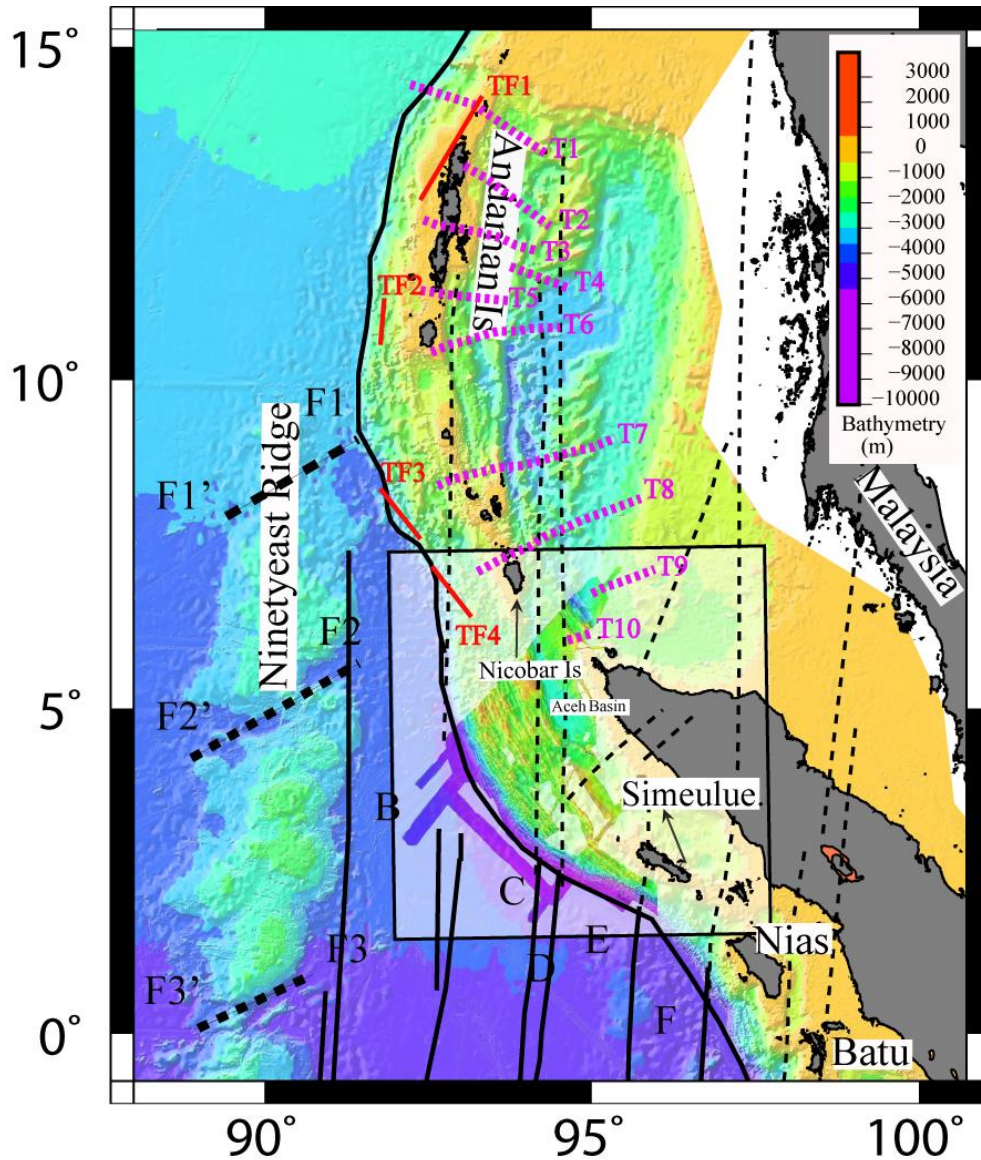


Figure 8: The satellite bathymetry (GEBCO) of the subducting Northern Wharton basin lithosphere is superimposed by the high-resolution bathymetry (edited version from Graindorge et al., 2008) highlighted in black box. Thick dashed lines on the Ninety East Ridge represents the location of *en-echelon* faults F1-F1', F2-F2', F3-F3' (after Subrahmanyam et al., 2008). The purple dashed line represents the tear faults T1-T10 (Dasgupta et al. 2003; Mukhopadhyay et al. 2009). The solid red line represents the trans-tensional strike-slip faults TF1-Tf4 (Mukhopadhyay et al. 2016). Details of the fracture zones and focal mechanisms are same as Figure 5,6 and 7.

5.2 Fracture zone B-C

Fracture zone B-C separates lithospheric compartments with strong age, thickness, bulk density, and subductability contrasts. Submitted to simultaneous resistance for oblique subduction due to subductability contrast and compressional stress induced by the internal deformation, the lithosphere may preferentially break on such heterogeneity if properly oriented. Fracture Zone B-C meets the trench at $\sim 5^\circ$ N and displays an important cluster of strike-slip earthquakes within a depth range of 10 to 40 km. At ASSZ the subducting thicker lithosphere of compartment B have higher slab pull due to higher subductability. Contrary, the lower subductability of compartment C experience lower slab pull. Hence the seismic coupling along the Fracture zone B-C due to subductability contrast between compartment B and C ($\sim 0.683 \times 10^9 \text{ Nm}^{-2}$) is higher, which is manifested as strike-slip earthquakes extending up to $\sim 1^\circ$ S. In future, the probable chances for the seismicity to extend further southward along the Fracture Zone BC is maximum until the subductability contrast is reduced. However, with the progression of subduction the differential slab pull may initiate slab tearing and the seismic coupling along the Fracture zone B-C will retard, once the tearing is initiated. The tearing may happen vertically along the fracture zone or horizontally across the slab leading to slab detachment. Currently there is no tearing reported along the Fracture zone B-C. The schematic representation of the differential slab pull caused by the strong subductability contrast between the Compartment B and C is shown in Figure 9.

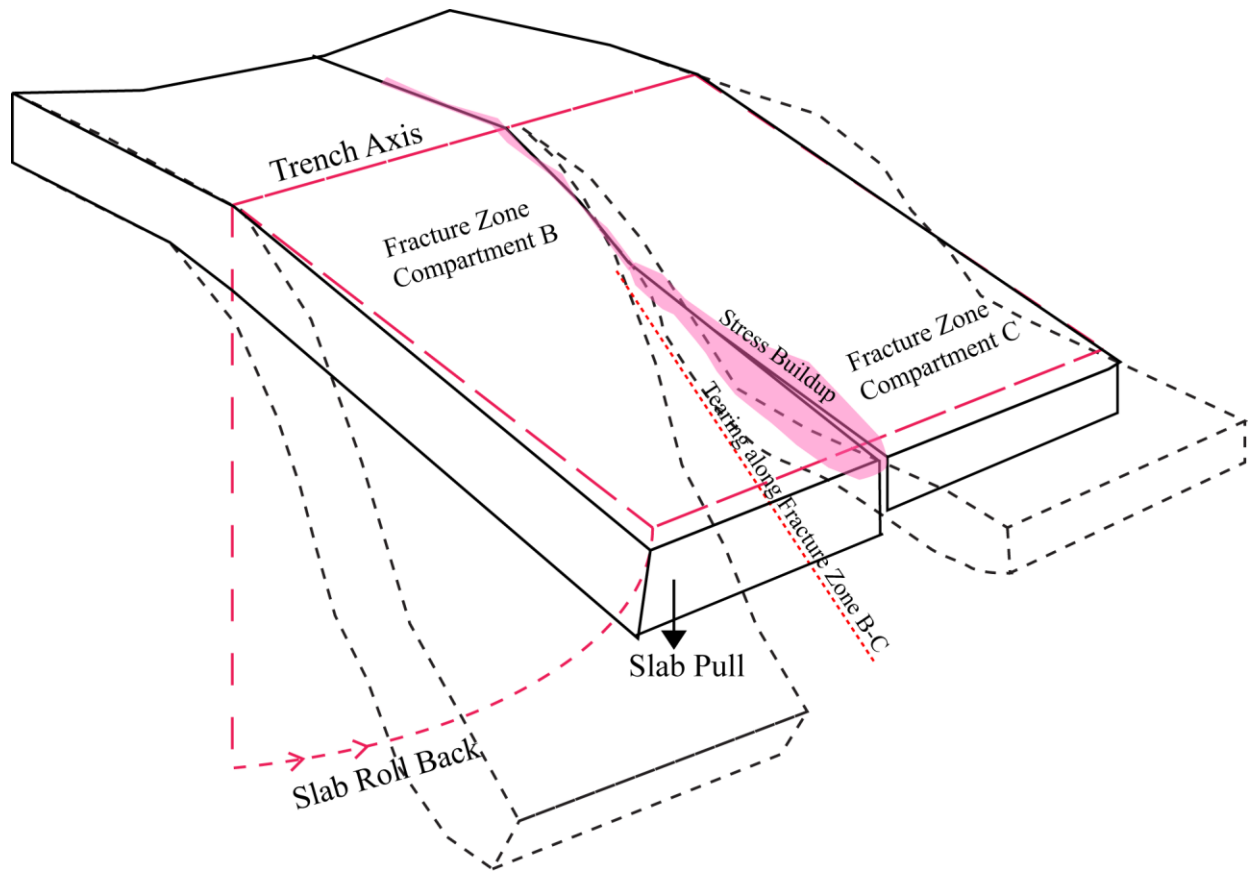


Figure 9: Schematic representation of the stress buildup due to the subductability contrast along the Fracture Zone B-C. The solid black line represents the current position of the subducting lithosphere and the dashed black line represents the subducting slab after the tearing. Due to the differential slab pull by the thicker/denser lithosphere of Compartment B and thinner/lighter lithosphere of the Compartment C, the stress along the Fracture Zone B-C increases causing strike-slip earthquakes. Eventually with the advancement of subduction, the increasing slab pull will lead to the tearing of the lithosphere along the prevalent fracture zone providing the provision to release the accumulated stress and prevent further stress buildup.

5.3 Compartments C, D, E and F

No cluster of strike slip earthquake is observed in Compartments C and D. Conversely, a small cluster of strike-slip earthquakes is observed on the accretionary island of Simeulue, above subducting Compartments E and F. An event, 20-30 km deep, is located in Compartment E whereas the others are located in Compartment F. A small subductability difference of $\sim 0.04 \times 10^9 \text{ Nm}^{-2}$ is observed between Compartments E and F. The low subductability in Compartments E and F agrees with the shallow subduction imaged by seismic tomography (Pesicek et al., 2008; 2010; Hall and Spakman, 2015). The higher resistance to subduction means more compression within the accretionary prism, causing stress rearrangements (e.g. Saffer and Tobin, 2011) along steeply

dipping faults within the accretionary prism (Singh et al., 2012; Ghosal et al., 2014) accounting for the shallow earthquakes. Hananto (2011) imaged the subducting plate below Simeulue Island down to ~35 km, suggesting that the deeper earthquakes showing both left- and right-lateral motions originate in the lower crust or the upper mantle. Most of the strike-slip earthquakes are roughly aligned on the reconstructed Fracture Zones E-F and F-G. Briggs et al. (2006) interpret a saddle-shaped depression including Simeulue and Nias Islands region as reflecting lithospheric tearing, whereas seismic tomography (Pesicek et al., 2008; 2010) suggests that it may instead represent the surface expression of a slab fold. We propose that the reactivation of Fracture Zone E-F between these islands caused a local depression bounded by the elevated flanks of the fracture zones (Figure 10). In this respect, the structure and physical properties of the subducting plate influence deformation of the overriding plate (e.g., Graindorge et al, 2008).

Though the nominal subductability contrast between the compartment C and D is our primary diagnosis for no or feeble seismicity along the fracture Zone C-D and D-E, we also propose the possibility of horizontal tearing and slab break-off of the oldest trailing edges of Compartment C and D due to the increasing slab pull cause by the thicker lithosphere (Figure 10), beneath the Andaman Sea. The upwelling of hot asthenosphere mantle along the horizontal tear may mimics a back arc spreading setup. A sub horizontal tear (e.g., Richards et al. 2007; Singh and Moeremans, 2017) on the steeply dipping subducting slab (Shapiro et al. 2008) beneath the Andaman sea is already been proposed, which is evidenced by the unusual perpendicular orientation of the Andaman Sea spreading axis with respect to the Sunda trench. The spreading axis could be the initial location of necking and final tearing of the lithosphere. The closer location and the comparable width of the reconstructed Fracture zones B-C, C-D and D-E with the Andaman Sea transform faults BC', CD' and DE' shows a considerable correlation.

Similarly, the presence of another localized tearing is imaged at ~20°, below the north of Burma (Pesicek et al., 2008; 2010), reflecting the separation between the upper-mantle slab below Burma (Huang & Zhao, 2006). Previously, the tear has been proposed as the relict of subduction zone along late Mesozoic South China Trench (Li et al., 2008b). However, we propose the possibility of horizontal tearing and the eventual slab break off of the trailing older lithosphere of the Compartment E and F at this location (Figure 10).

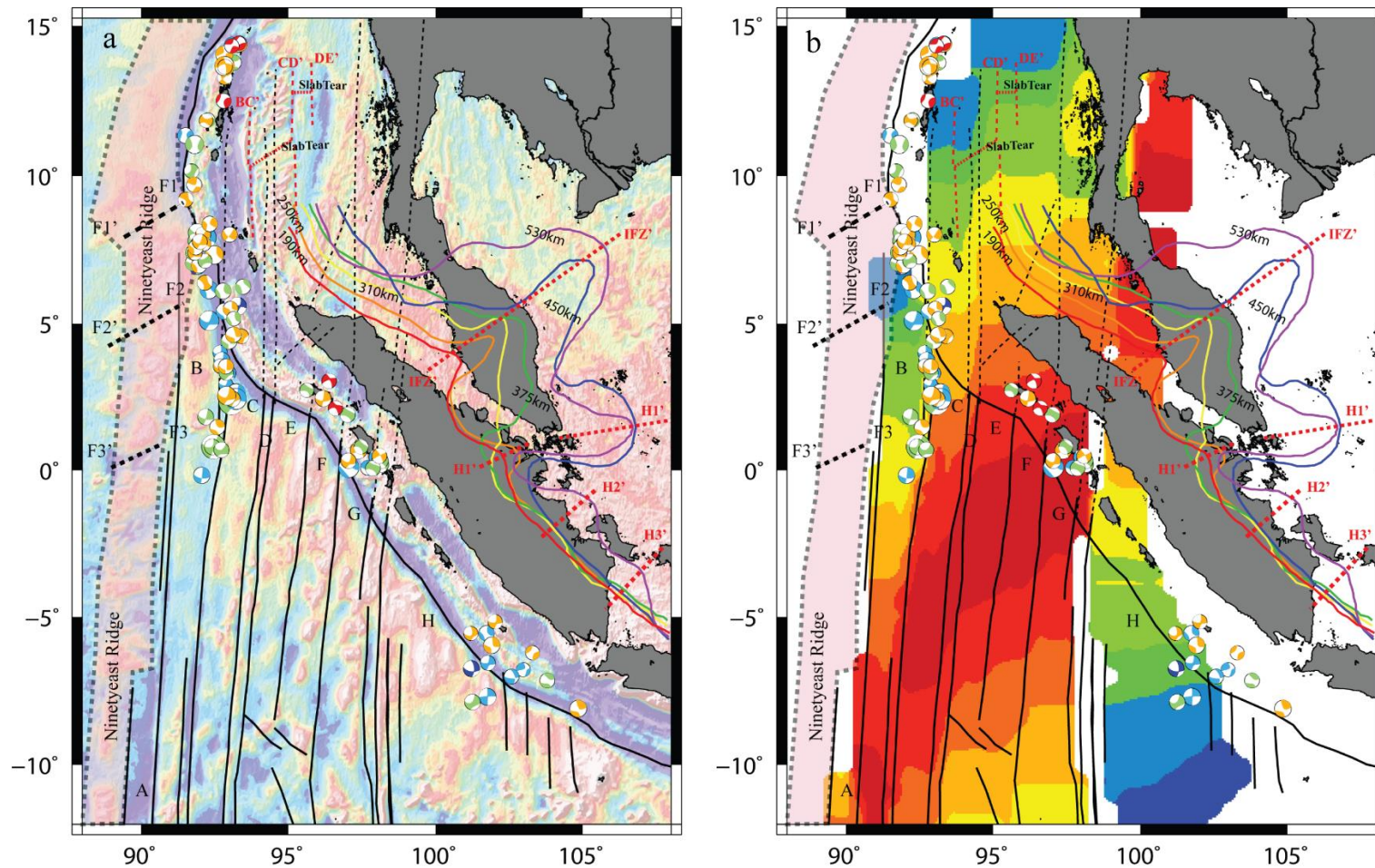


Figure 10: Depth contours imaged by Pesicek et al., 2008; 2010 is superimposed on a) free air gravity anomaly derived from satellite altimetry (Sandwell et al., 2014) b) age grid of the Wharton lithosphere. The red dashed lines BC', CD' and DE' represents the actual location of the transform faults associated with the Andaman Sea spreading. IFZ', H1', H2' and H3' marks the hinges of the folds on the depth contours of the subducting slab.

5.4 Compartment G

The resistance offered by the lithosphere to subduction is the highest of the area in Compartment G, showing the lowest subductability value of $\sim 2.18 \times 10^9 \text{ Nm}^{-2}$ for an age as young as $\sim 36 \text{ Ma}$ (Jacob et al., 2014). The seismicity on this compartment, in a depth range of 10-40 km, is not aligned along fracture zone F-G and the Investigator Fracture Zone, but instead is distributed within Compartment G.

The shallower seismicity within 5-20 km depth is more probably controlled by dehydration, compaction and draining of the pore fluid from the accreted sediments in the prism (Faccenda, 2014; Saffer and Tobin, 2011; Hyndman and Peacock, 2003) that generate earthquakes on the high angle dipping faults bounding steeply dipping wedges of sediments (Singh et al., 2012; Ghosal et al., 2014).

As for the deeper seismicity, the lithosphere of Compartment G formed at a slow to ultra-slow spreading center (Jacob et al, 2014), usually characterized by outcropping gabbro and serpentinitized peridotite (Cannat et al, 1993; Smith et al, 2008, Whitney et al; 2013). The deeper earthquakes may therefore be caused by dehydration of the subducting slab (e.g., Paulatto et al, 2017) involving the transition to blueschist-eclogite facies and, deeper, the de-serpentinization of lithospheric mantle (Hacker et al, 2003). Although a slab window has been considered in this location (e.g., Whittaker et al., 2007), no evidence of tearing appears on regional seismic tomography (Pesicek et al., 2008; 2010).

5.5 Compartment H

The wide Compartment H is bounded by the Investigator Fracture Zone (IFZ) on the west and several fracture zones on the eastern side. No strike-slip earthquakes are aligned along the IFZ, while the eastern fracture zones show strike-slip earthquakes between 10 and 40 km. The subductability contrast between Compartments H and G ($\sim 1.2 \times 10^9 \text{ Nm}^{-2}$; Figure 5) is higher than that of Compartments B and C. The folding imaged on the subducting lithosphere by Pesicek et al., 2008; 2010 dated $\sim 17 \text{ My}$ is possibly an impression of the subducted IFZ (IFZ' of Figure 10). Similar folding is observed at the southern Central America where the subducting slab of Cocos and Nazca plate have an age difference of $\sim 5 \text{ Ma}$ (Protti et al. 1994). Conventionally, the higher subductability contrast between the lithosphere in Compartment G and H, separated by the IFZ expected to display higher strike-slip earthquakes. But despite of the highest subductability

contrast no strike-slip earthquakes are recorded along the IFZ. Later, the tomography interpreted by Chesner, 2012; Hall and Spakman, 2015 proposed the tearing of the subducted lithosphere beneath volcanic center of Toba, instead of slab folding. The slab tearing has possibly retarded the nucleation of strike slip earthquakes along IFZ. The lack of seismicity along the IFZ may also result from its segmentation into four elongated NS-trending segments. Conversely, it may also reflect a bias in our strike-slip earthquake sampling, as no major subduction earthquake has excited this part of the slab during the last 15 years investigated in this study.

The fracture zones on the eastern side of the Compartment H separates the older lithosphere of the western Australian basins. Hence, we expect higher subductability contrast which is manifested as strike-slip earthquakes along the eastern fracture zones of the Compartment H. The folding imaged by Pesicek tomography model shows small related foldings towards the eastern side of the IFZ (H1', H2' and H3' of Figure 10). We associate these with the subduction of the multiple eastern fracture zones of the Compartment H. The hinges of the imaged folds H1', H2' and H3' shows northeast-southwest orientation indicating an oblique subduction of the lithosphere east of the IFZ. This may be due to the excess slab-pull exerted by the thicker and denser subducting lithosphere of the Compartment H. The lower subduction angle ($\sim 25^{\circ}$ to 60° ; by Pesicek et al., 2008; Kennett and Cummins, 2005; Shapiro et al., 2008) for the subducting lithosphere on west of the IFZ reflects the younger lithospheric age with lower slab-pull. The differential slab pulls on either side of the IFZ have teared the subducting slab on either side of the IFZ.

6. Conclusions

We quantify physical parameters and define subductability in each compartment of the Wharton Basin lithosphere to investigate the influence of subductability contrasts in generating the strike-slip seismicity along the ASSZ.

1. Lithospheric thickness and bulk density are estimated from the age of the lithosphere in the Wharton Basin, and 'subductability', a parameter to represent the easiness of lithospheric subduction is further estimated from these parameters.
2. The stress accumulation along the fracture zones caused by the differential slab-pull due to the subductability contrast between the subducting lithospheric compartments is manifested as strike-slip earthquakes along the fracture zones of the Wharton basin.

3. With the progression of subduction, the increasing slab pull may culminate in tearing the subducting lithosphere, releasing the accumulated stress.
4. The strike-slip seismicity is maximum along Fracture Zone A-B where the Ninety East Ridge interacts with the ASSZ at $\sim 5^\circ$ N.
5. A high subductability contrast is observed between Compartment B and C, dominated by left-lateral strike-slip partitioning along the fracture zones. The seismicity along the Fracture zone B-C may continue inside the Wharton basin until the subductability contrast is reduced or the stress is released by any slab tearing.
6. The shallow strike slip earthquakes beneath Simeulue and Nias Islands reflect local geometric rearrangements within the accretionary prism favored by the lower subductability and stronger resistance to subduction of the Compartments C, D, E and F. The deeper earthquakes reflect rejuvenation of the subducting fracture zones.
7. A cluster of strike-slip earthquakes in Compartment G, parallel to the trench, may result from the dehydration of serpentized lithosphere formed at slow to ultra-slow spreading (deserpentinization).
8. Despite a high subductability contrast between Compartments H and G, slab tearing along the subducting IFZ prevents stress accumulation and earthquake generation on this fracture zone.
9. Contrasts of lithospheric subductability between the compartments of the subducting Wharton Basin and the Ninety East Ridge along the ASSZ is represented schematically in Figure 11.

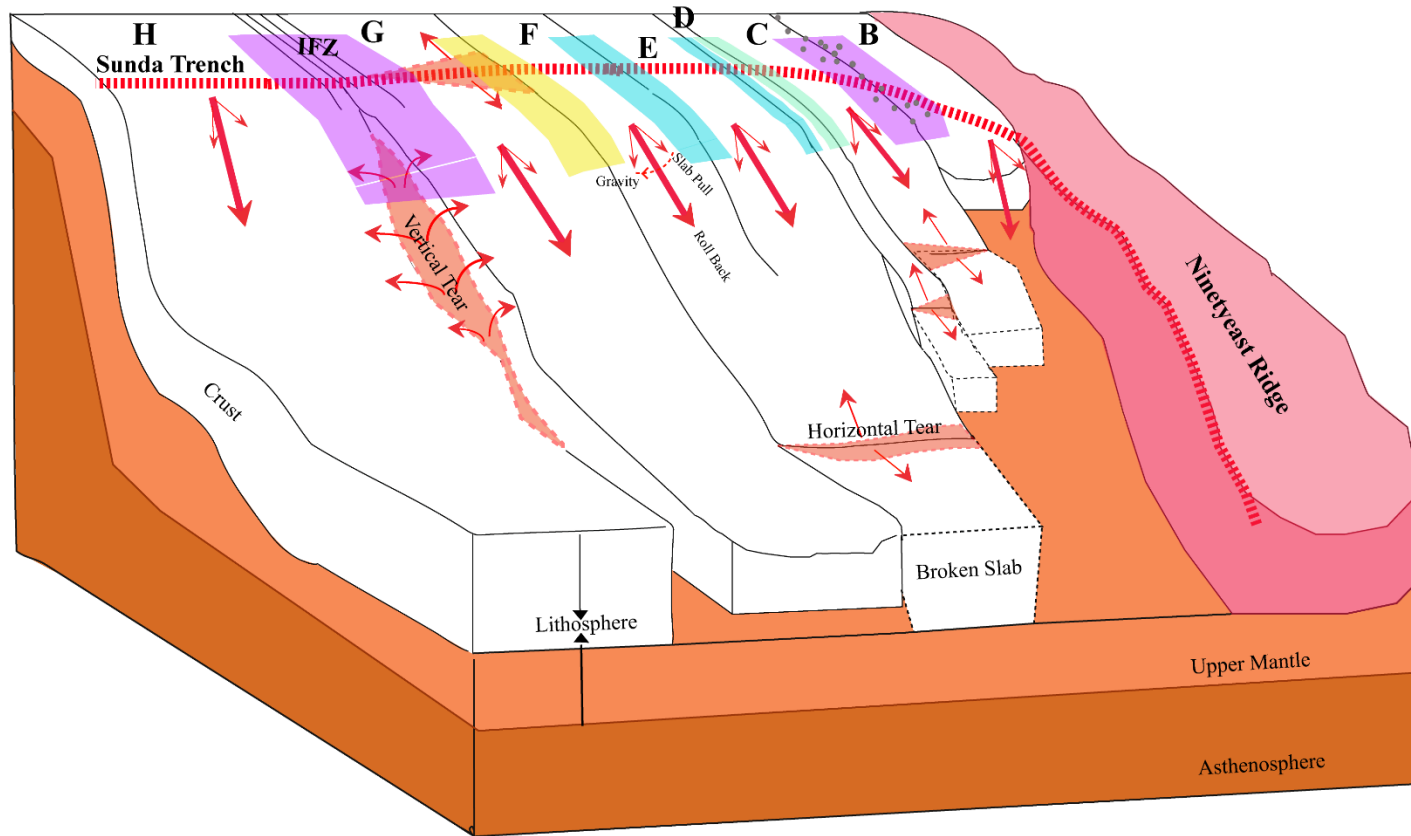


Figure 11: The schematic representation of the subducting northern Wharton lithosphere at the Sunda Trench. The subductability contrast between each lithospheric compartment is represented in different color code; purple-High, light green- medium, light blue-low, yellow-lowest. Black dots represent the strike-slip earthquakes along the Fracture Zone B-C due to the high subductability contrast between the fracture zone Compartments B and C. Though a higher subductability contrast is observed between the Compartment G and H, the vertical tearing along the IFZ (Chesner, 1998, 2012) prevents the stress accumulation and associated seismicity. The horizontal tear (Richards et al. 2007; Singh and Moeremans, 2017) formed by the slab break off due to the excess slab pull at the older edges of Compartment C and D might have initiated the spreading in the Andaman Sea. The horizontal tear proposed in the Compartment E-F corresponds to the tearing under the Burma plate (Pesicek et al., 2008; 2010).

Acknowledgement

The authors thank the Director, CSIR-National Institute of Oceanography, Goa for the support to carry out this work. Jensen Jacob is grateful to Dr. David Graindorge and the anonymous reviewer for their constructive comments and suggestions which helped to elevate the quality of the manuscript. This research was carried out on internal funding. This is NIO contribution XXXX and IGP contribution XXXX

Data Availability

The earthquake focal mechanism used in this study have been obtained from The Global Centroid Moment Tensor Project at <https://www.globalcmt.org/CMTsearch.html> and the marine magnetic data used to derive the age of the oceanic lithosphere are available from the National Centers for Environmental Information at <https://www.ngdc.noaa.gov/mgg/geodas/>

Author contributions

Jensen Jacob: Conception, Methodology, Formal analysis, Investigation, Writing - Original Draft. Jérôme Dymont: Conception, Methodology, Writing - Review & Editing. Dibakar Ghosal: Writing - Review & Editing. Pawan Dewangan: Writing - Review & Editing

References

- Abercrombie, R.E., Antolik, M., Ekström, G., 2003. The June 2000 Mw 7.9 earthquakes south of Sumatra: Deformation in the India-Australia Plate. *J. Geophys. Res. Solid Earth* 108, ESE 6-1-ESE 6-16. <https://doi.org/10.1029/2001jb000674>
- Bergman, E.A., Solomon, S.C., 1985. Earthquake source mechanisms from body-waveform inversion and intraplate tectonics in the northern Indian Ocean. *Phys. Earth Planet. Inter.* 40, 1–23. [https://doi.org/10.1016/0031-9201\(85\)90002-0](https://doi.org/10.1016/0031-9201(85)90002-0)
- Briggs, R.W., Sieh, K., Meltzner, A.J., Natawidjaja, D., Galetzka, J., Suwargadi, B., Hsu, Y., Simons, M., Hananto, N., Suprihanto, I., Prayudi, D., Avouac, J., Prawirodirdjo, L., Bock, Y., 2006. Deformation and Slip Along the the Sunda Megathrust in the Great 2005 Nias-Simeulue. *Science* 311, 1897–1901.
- Bull, J.M., Scrutton, R.A., 1990. Fault reactivation in the Central Indian Ocean and the rheology of the oceanic lithosphere. *Nature* 334, 855-858.
- Cande, S.C., Kent, D. V, 1995. Revised calibration of the geomagnetic polarity timescale for the late Cretaceous and Cenozoic. *J. Geophys. Res.* 100, 6093–6095. <https://doi.org/10.1029/94JB03098>
- Cannat, M., 1993. Emplacement of mantle rocks in the seafloor at mid-ocean ridges. *J. Geophys. Res.* 98, 4163–4172. <https://doi.org/10.1029/92JB02221>
- Carlson, R.L., Herrick, C.N., 1990. Densities and porosities in the oceanic crust and their variations with depth and age. *J. Geophys. Res.* 95, 9153–9170. <https://doi.org/10.1029/JB095iB06p09153>
- Carton, H., Singh, S.C., Hananto, N.D., Martin, J., Djajadihardja, Y.S., Udrek, Franke, D., Gaedicke, C., 2014. Deep seismic reflection images of the Wharton Basin oceanic crust and uppermost mantle offshore Northern Sumatra: Relation with active and past deformation. *J. Geophys. Res. Solid Earth* 119, 32–51. <https://doi.org/10.1002/2013JB010291>
- Cattin, R., Chamot-Rooke, N., Pubellier, M., Rabaute, A., Delescluse, M., Vigny, C., Fleitout, L., Dubernet, P., 2009. Stress change and effective friction coefficient along the Sumatra-Andaman-Sagaing fault system after the 26 December 2004 (Mw = 9.2) and the 28 March 2005 (Mw = 8.7) earthquakes. *Geochemistry, Geophys. Geosystems* 10. <https://doi.org/10.1029/2008GC002167>
- Chamot-Rooke, N., F. Jestin, B. De Voogd, J. Diebold, J. Dymant, F. Farcy, L. Fleitout, P. Huchon, P. Liverpool, M. Munsch, A. Oshida, J.-Y. Royer, C. Truffert, J. K. Weissel, A. Ziolkowski, A., 1993. Intraplate shortening in the central Indian-ocean determined from a 2100-Km-long North-South deep seismic-reflection profile. *Geology*, 21, 1043-1046.
- Chesner, C.A., 2012. The Toba caldera complex. *Quat. Int.* 258, 5–18.

- Chlieh, M., Avouac, J.-P., Hjorleifsdottir, V., Song, T.-R.A., Ji, C., Sieh, K., Sladen, A., Hebert, H., Prawirodirdjo, L., Bock, Y., Galetzka, J., 2007. Coseismic Slip and Afterslip of the Great Mw 9.15 Sumatra-Andaman Earthquake of 2004. *Bull. Seismol. Soc. Am.* 97, S152–S173. <https://doi.org/10.1785/0120050631>
- Cloetingh, S., Wortel, R., 1985. Regional stress field of the Indian Plate. *Geophys. Res. Lett.* 12, 77–80. <https://doi.org/10.1029/GL012i002p00077>
- Coblentz, D.D., Zhou, S., Hillis, R.R., Richardson, R.M., Sandiford, M., 1998. Topography, boundary forces, and the Indo-Australian intraplate stress field. *J. Geophys. Res. Solid Earth* 103, 919–931. <https://doi.org/10.1029/97jb02381>
- Dasgupta, S., Mukhopadhyay, M., Bhattacharya, A., Jana, T.K., 2003. The geometry of the Burmese-Andaman subducting lithosphere. *J. Seismol.* 7, 155–174. <https://doi.org/10.1023/A:1023520105384>
- Delescluse, M., Chamot-Rooke, N., 2007. Instantaneous deformation and kinematics of the India-Australia Plate. *Geophys. J. Int.* 168, 818–842. <https://doi.org/10.1111/j.1365-246X.2006.03181.x>
- Delescluse, M., Chamot-Rooke, N., Cattin, R., Fleitout, L., Trubienko, O., Vigny, C., 2012. April 2012 intra-oceanic seismicity off Sumatra boosted by the Banda-Aceh megathrust. *Nature* 490, 240–244. <https://doi.org/10.1038/nature11520>
- DeMets, C., Gordon, R.G., Royer, J.Y., 2005. Motion between the Indian, Capricorn and Somalian plates since 20 Ma: Implications for the timing and magnitude of distributed lithospheric deformation in the equatorial Indian ocean. *Geophys. J. Int.* 161, 445–468. <https://doi.org/10.1111/j.1365-246X.2005.02598.x>
- Deplus, C., 2001. Indian Ocean Actively Deforms. *Science* 292, 1850–1851.
- Deplus, C., Diament, M., Hébert, H., Bertrand, G., Dominguez, S., Dubois, J., Malod, J., Patriat, P., Pontoise, B., Sibilla, J.J., 1998. Direct evidence of active deformation in the eastern Indian oceanic plate. *Geology* 26, 131–134.
- Doin, M.P., Fleitout, L., 1996. Thermal evolution of the oceanic lithosphere: An alternative view. *Earth Planet. Sci. Lett.* 142, 121–136. [https://doi.org/10.1016/0012-821x\(96\)00082-9](https://doi.org/10.1016/0012-821x(96)00082-9)
- Duputel, Z., Kanamori, H., Tsai, V.C., Rivera, L., Meng, L., Ampuero, J.P., Stock, J.M., 2012. The 2012 Sumatra great earthquake sequence. *Earth Planet. Sci. Lett.* 351–352, 247–257. <https://doi.org/10.1016/j.epsl.2012.07.017>
- Dziewonski, A.M., Chou, T.A., Woodhouse, J.H., 1981. Determination of earthquake source parameters from waveform data for studies of global and regional seismicity. *J. Geophys. Res.* 86, 2825–2852. <https://doi.org/10.1029/JB086iB04p02825>
- Engdahl, E.R., Villaseñor, A., DeShon, H.R., Thurber, C.H., 2007. Teleseismic relocation and assessment of seismicity (1918-2005) in the region of the 2004 Mw 9.0 Sumatra-Andaman and 2005 Mw 8.6 Nias Island great earthquakes. *Bull. Seismol. Soc. Am.* 97. <https://doi.org/10.1785/0120050614>

- Ekström, G., Nettles, M., Dziewoński, A.M., 2012. The global CMT project 2004-2010: Centroid-moment tensors for 13,017 earthquakes. *Phys. Earth Planet. Inter.* 200–201, 1–9. <https://doi.org/10.1016/j.pepi.2012.04.002>
- Faccenda, M., 2014. Water in the slab: A trilogy. *Tectonophysics* 614, 1–30. <https://doi.org/10.1016/j.tecto.2013.12.020>
- Fullerton, L.G., Sager, W.W., Handschumacher, D.W., 1989. Late Jurassic-Early Cretaceous evolution of the eastern Indian Ocean adjacent to northwest Australia. *J. Geophys. Res.* 94, 2937–2953. <https://doi.org/10.1029/JB094iB03p02937>
- Gahalaut, V.K., Subrahmanyam, C., Kundu, B., Catherine, J.K., Ambikapathy, A., 2010. Slow rupture in andaman during 2004 Sumatra-Andaman earthquake: A probable consequence of subduction of 90°E ridge. *Geophys. J. Int.* 180, 1181–1186. <https://doi.org/10.1111/j.1365-246X.2009.04449.x>
- Geersen, J., Bull, J.M., McNeill, L.C., Henstock, T.J., Gaedicke, C., Chamot-Rooke, N., Delescluse, M., 2015. Pervasive deformation of an oceanic plate and relationship to large > Mw 8 intraplate earthquakes: The northern Wharton Basin, Indian Ocean. *Geology* 43, 359–362. <https://doi.org/10.1130/G36446.1>
- Ghosal, D., Singh, S.C., Martin, J., 2014. Shallow subsurface morphotectonics of the NW Sumatra subduction system using an integrated seismic imaging technique. *Geophys. J. Int.* 198, 1818–1831. <https://doi.org/10.1093/gji/ggu182>
- Gordon, R.G., DeMets, C., Royer, J.Y., 1998. Letters to nature. *Nature* 395, 370–374. <https://doi.org/10.1038/26463>
- Graindorge, D., Klingelhoefer, F., Sibuet, J.C., McNeill, L., Henstock, T.J., Dean, S., Gutscher, M.A., Dessa, J.X., Permana, H., Singh, S.C., Leau, H., White, N., Carton, H., Malod, J.A., Rangin, C., Aryawan, K.G., Chaubey, A.K., Chauhan, A., Galih, D.R., Greenroyd, C.J., Laesanpura, A., Prihantono, J., Royle, G., Shankar, U., 2008. Impact of lower plate structure on upper plate deformation at the NW Sumatran convergent margin from seafloor morphology. *Earth Planet. Sci. Lett.* 275, 201–210. <https://doi.org/10.1016/j.epsl.2008.04.053>
- Hacker, B.R., Peacock, S.M., Abers, G.A., Holloway, S.D., 2003. Subduction factory 2. Are intermediate-depth earthquakes in subducting slabs linked to metamorphic dehydration reactions? *J. Geophys. Res. Solid Earth* 108. <https://doi.org/10.1029/2001jb001129>
- Hall, R., Spakman, W., 2015. Mantle structure and tectonic history of SE Asia. *Tectonophysics* 658, 14–45. <https://doi.org/10.1016/j.tecto.2015.07.003>
- Hananto, N., Boudarine, A., Carton, H., Singh, S.C., Avianto, P., Dymant, J., Qin, Y., Ghosal, D., Zuraida, R., Tapponnier, P.E., Deplus, C., Sieh, K., 2018. Evidence of pervasive trans-tensional deformation in the northwestern Wharton Basin in the 2012 earthquakes rupture area. *Earth Planet. Sci. Lett.* 502, 174–186. <https://doi.org/10.1016/j.epsl.2018.09.007>

- Hananto, N., PhD Thesis 2011, Institut de physique du globe (Paris); Architecture and Evolution of North Sumatra Subduction Zone based on long Offset Seismic Reflection and Wide Angle Seismic Refraction / Reflection Data
- Hasterok, D., 2013. A heat flow based cooling model for tectonic plates. *Earth Planet. Sci. Lett.* 361, 34–43. <https://doi.org/10.1016/j.epsl.2012.10.036>
- Hensen, C., Duarte, J.C., Vannucchi, P., Mazzini, A., Lever, M.A., Terrinha, P., Géli, L., Henry, P., Villinger, H., Morgan, J., Schmidt, M., Gutscher, M.A., Bartolome, R., Tomonaga, Y., Polonia, A., Gràcia, E., Tinivella, U., Lupi, M., Çağatay, M.N., Elvert, M., Sakellariou, D., Matias, L., Kipfer, R., Karageorgis, A.P., Ruffine, L., Liebetrau, V., Pierre, C., Schmidt, C., Batista, L., Gasperini, L., Burwicz, E., Neres, M., Nuzzo, M., 2019. Marine transform faults and fracture zones: A joint perspective integrating seismicity, fluid flow and life. *Front. Earth Sci.* 7, 1–29. <https://doi.org/10.3389/feart.2019.00039>
- Hyndman, R.D., Peacock, S.M., 2003. Serpentinization of the forearc mantle. *Earth Planet. Sci. Lett.* 212, 417–432. [https://doi.org/10.1016/S0012-821X\(03\)00263-2](https://doi.org/10.1016/S0012-821X(03)00263-2)
- Huang, J., Zhao, D., 2006. High-resolution mantle tomography of China and surrounding regions. *J. Geophys. Res. Solid Earth* 111, 1–21. <https://doi.org/10.1029/2005JB004066>
- Ishii, M., Kiser, E., Geist, E.L., 2013. Mw 8.6 Sumatran earthquake of 11 April 2012: Rare seaward expression of oblique subduction. *Geology* 41, 319–322. <https://doi.org/10.1130/G33783.1>
- Jacob, J., Dymant, J., Yatheesh, V., 2014. Revisiting the structure, age, and evolution of the Wharton Basin to better understand subduction under Indonesia. *J. Geophys. Res. Solid Earth* 119, 169–190. <https://doi.org/10.1002/2013JB010285>
- Kennett, B.L.N., Cummins, P.R., 2005. The relationship of the seismic source and subduction zone structure for the 2004 December 26 Sumatra-Andaman earthquake. *Earth Planet. Sci. Lett.* 239, 1–8. <https://doi.org/10.1016/j.epsl.2005.08.015>
- Korenaga, T., Korenaga, J., 2008. Subsidence of normal oceanic lithosphere, apparent thermal expansivity, and seafloor flattening. *Earth Planet. Sci. Lett.* 268, 41–51. <https://doi.org/10.1016/j.epsl.2007.12.022>
- Lay, T., 2019. Reactivation of Oceanic Fracture Zones in Large Intraplate Earthquakes?, in: *Transform Plate Boundaries and Fracture Zones*. Elsevier, pp. 89–104. <https://doi.org/10.1016/B978-0-12-812064-4.00004-9>
- Lay, T., Wallace, T.C., 1995. Modern global seismology, in: Lay, T., W (Eds.), . Academic Press An Imprint of Elsevier 525 B Street, Suite 1900, San Diego, California 92101-4495, USA <http://www.academicpress.com>, p. 521.
- Lay, T., Ye, L., Ammon, C.J., Dunham, A., Koper, K.D., 2016. The 2 March 2016 Wharton Basin Mw 7.8 earthquake: High stress drop north-south strike-slip rupture in the diffuse oceanic deformation zone between the Indian and Australian Plates. *Geophys. Res. Lett.* 43, 7937–

7945. <https://doi.org/10.1002/2016GL069931>
- Li, C., van der Hilst, R.D., Meltzer, A.S., Engdahl, E.R., 2008. Subduction of the Indian lithosphere beneath the Tibetan Plateau and Burma. *Earth Planet. Sci. Lett.* 274, 157–168. <https://doi.org/10.1016/j.epsl.2008.07.016>
- Lin, J.Y., Le Pichon, X., Rangin, C., Sibuet, J.C., Maury, T., 2009. Spatial aftershock distribution of the 26 December 2004 great Sumatra-Andaman earthquake in the northern Sumatra area. *Geochemistry, Geophys. Geosystems* 10. <https://doi.org/10.1029/2009GC002454>
- Liu, C.S., Curray, J.R., McDonald, J.M., 1983. New constraints on the tectonic evolution of the eastern Indian Ocean. *Earth Planet. Sci. Lett.* 65, 331–342. [https://doi.org/10.1016/0012-821X\(83\)90171-1](https://doi.org/10.1016/0012-821X(83)90171-1)
- McAdoo, D.C., Sandwell, D.T., 1985. Folding of oceanic lithosphere. *J. Geophys. Res.* 90, 8563–8569. <https://doi.org/10.1029/JB090iB10p08563>
- McGuire, J.J., Beroza, G.C., 2012. A rogue earthquake off Sumatra. *Science* (80-.). 336, 1118–1119. <https://doi.org/10.1126/science.1223983>
- McKenzie, D.P., 1967. Some remarks on heat flow and gravity anomalies. *J. Geophys. Res.* 72, 6261–6273. <https://doi.org/10.1029/jz072i024p06261>
- Meng, L., Ampuero, J.P., Stock, J., Duputel, Z., Luo, Y., Tsai, V.C., 2012. Earthquake in a maze: Compressional rupture branching during the 2012 Mw 8.6 Sumatra earthquake. *Science* (80-.). 337, 724–726. <https://doi.org/10.1126/science.1224030>
- Moeremans, R.E., Singh, S.C., 2014. Seismic evidence of continental margin influence on the NinetyEast Ridge in the Bay of Bengal. *Geophys. Res. Lett.* 41, 7143–7150. <https://doi.org/10.1002/2014GL061598>
- Mukhopadhyay, B., Acharyya, A., Bhattacharya, A., Dasgupta, S., Sengupta, S.R., 2009. Revisiting the Andaman subduction lithosphere following the 26 December 2004 Sumatra earthquake. *Indian Miner.* 63, 1–10.
- Mukhopadhyay, B., Dasgupta, S., Mukherjee, P., 2016. Slab tear and tensional fault systems in the Sunda–Andaman Benioff zone: implications on tectonics and potential seismic hazard. *Geomatics, Nat. Hazards Risk* 7, 1129–1146. <https://doi.org/10.1080/19475705.2015.1011242>
- Mukhopadhyay, M., Krishna, M.B.R., 1995. Gravity anomalies and deep structure of the Ninetyeast Ridge north of the equator, eastern Indian Ocean - a hot spot trace model. *Mar. Geophys. Res.* 17, 201–216. <https://doi.org/10.1007/BF01203426>
- Parsons, B., McKenzie, D., 1978. Mantle convection and the thermal structure of the plates. *J. Geophys. Res.* 83, 4485. <https://doi.org/10.1029/jb083ib09p04485>

- Parsons, B., Sclater, J.G., 1977. An analysis of the variation of ocean floor bathymetry and heat flow with age. *J. Geophys. Res.* 82, 803–827. <https://doi.org/10.1029/jb082i005p00803>
- Paulatto, M., Laigle, M., Galve, A., Charvis, P., Sapin, M., Bayrakci, G., Evain, M., Kopp, H., 2017. Dehydration of subducting slow-spread oceanic lithosphere in the Lesser Antilles. *Nat. Commun.* 8, 1–11. <https://doi.org/10.1038/ncomms15980>
- Pesicek, J.D., Thurber, C.H., Widiyantoro, S., Engdahl, E.R., DeShon, H.R., 2008. Complex slab subduction beneath northern Sumatra. *Geophys. Res. Lett.* 35, 1–5. <https://doi.org/10.1029/2008GL035262>
- Pesicek, J.D., Thurber, C.H., Widiyantoro, S., Zhang, H., DeShon, H.R., Engdahl, E.R., 2010. Sharpening the tomographic image of the subducting slab below Sumatra, the Andaman Islands and Burma. *Geophys. J. Int.* 182, 433–453. <https://doi.org/10.1111/j.1365-246X.2010.04630.x>
- Petroy, D.E., Wiens, D.A., 1989. Historical seismicity and implications for diffuse plate convergence in the northeast Indian Ocean. *J. Geophys. Res.* 94. <https://doi.org/10.1029/jb094ib09p12301>
- Prawirodirdjo, L., Bock, Y., Genrich, J.F., Puntodewo, S.S.O., Rais, J., Subarya, C., Sutisna, S., 2000. One century of tectonic deformation along the Sumatran fault from triangulation and Global Positioning System surveys. *J. Geophys. Res. Solid Earth* 105, 28343–28361. <https://doi.org/10.1029/2000jb900150>
- Protti, M., Gündel, F., McNally, K., 1994. The geometry of the Wadati-Benioff zone under southern Central America and its tectonic significance: results from a high-resolution local seismographic network. *Phys. Earth Planet. Inter.* 84, 271–287. [https://doi.org/10.1016/0031-9201\(94\)90046-9](https://doi.org/10.1016/0031-9201(94)90046-9)
- Radha Krishna, M., Sanu, T.D., 2002. Shallow seismicity, stress distribution and crustal deformation pattern. *J. Seismol.* 6, 25–41. <https://doi.org/10.1023/A:1014203306506>
- Richards, S., Lister, G., Kennett, B., 2007. A slab in depth: Three-dimensional geometry and evolution of the Indo-Australian plate. *Geochemistry, Geophys. Geosystems* 8, 1–11. <https://doi.org/10.1029/2007GC001657>
- Robinson, D.P., 2011. A rare great earthquake on an oceanic fossil fracture zone. *Geophys. J. Int.* 186, 1121–1134. <https://doi.org/10.1111/j.1365-246X.2011.05092.x>
- Royer, J.Y., Gordon, R.G., 1997. The motion and boundary between the Capricorn and Australian plates. *Science* . 277, 1268–1274. <https://doi.org/10.1126/science.277.5330.1268>
- Sager, W.W., Bull, J.M., Krishna, K.S., 2013. Active faulting on the Ninetyeast Ridge and its relation to deformation of the Indo-Australian plate. *J. Geophys. Res. Solid Earth* 118, 1–12. <https://doi.org/10.1002/jgrb.50319>

- Saffer, D.M., Tobin, H.J., 2011. Hydrogeology and Mechanics of Subduction Zone Forearcs: Fluid Flow and Pore Pressure. *Annu. Rev. Earth Planet. Sci.* 39, 157–186. <https://doi.org/10.1146/annurev-earth-040610-133408>
- Sandwell, D.T., Müller, R.D., Smith, W.H.F., Garcia, E., Francis, R., 2014. New global marine gravity model from CryoSat-2 and Jason-1 reveals buried tectonic structure. *Science* 346, 65–67. <https://doi.org/10.1126/science.1258213>
- Satriano, C., Kiraly, E., Bernard, P., Vilotte, J.P., 2012. The 2012 Mw 8.6 Sumatra earthquake: Evidence of westward sequential seismic ruptures associated to the reactivation of a N-S ocean fabric. *Geophys. Res. Lett.* 39, 1–6. <https://doi.org/10.1029/2012GL052387>
- Sclater, J.G., Francheteau, J., 1970. The Implications of Terrestrial Heat Flow Observations on Current Tectonic and Geochemical Models of the Crust and Upper Mantle of the Earth. *Geophys. J. R. Astron. Soc.* 20, 509–542. <https://doi.org/10.1111/j.1365-246X.1970.tb06089.x>
- Shamim, S., Khan, P.K., Mohanty, S.P., Mohanty, M., 2021. Andaman–Nicobar–Sumatra Margin Revisited: Analysis of the Lithospheric Structure and Deformation Based on Gravity Modeling and Distribution of Seismicity. *Surv. Geophys.* <https://doi.org/10.1007/s10712-021-09633-9>
- Shapiro, N.M., Ritzwoller, M.H., Engdahl, E.R., 2008. Structural context of the great Sumatra–Andaman Islands earthquake. *Geophys. Res. Lett.* 35, 1–5. <https://doi.org/10.1029/2008GL033381>
- Singh, S.C., Chauhan, A.P.S., Calvert, A.J., Hananto, N.D., Ghosal, D., Rai, A., Carton, H., 2012. Seismic evidence of bending and unbending of subducting oceanic crust and the presence of mantle megathrust in the 2004 Great Sumatra earthquake rupture zone. *Earth Planet. Sci. Lett.* 321–322, 166–176. <https://doi.org/10.1016/j.epsl.2012.01.012>
- Singh, S.C., Hananto, N., Qin, Y., Leclerc, F., Avianto, P., Tapponnier, P.E., Carton, H., Wei, S., Nugroho, A.B., Gemilang, W.A., Sieh, K., Barbot, S., 2017. The discovery of a conjugate system of faults in the wharton basin intraplate deformation zone. *Sci. Adv.* 3, 1–9. <https://doi.org/10.1126/sciadv.1601689>
- Singh, S.C., Moeremans, R., 2017. Anatomy of the Andaman–Nicobar subduction system from seismic reflection data. *Geol. Soc. Mem.* 47, 193–204. <https://doi.org/10.1144/M47.13>
- Smith, D.K., Escartín, J., Schouten, H., Cann, J.R., 2008. Fault rotation and core complex formation: Significant processes in seafloor formation at slow-spreading mid-ocean ridges (Mid-Atlantic Ridge, 13°–15°N). *Geochemistry, Geophys. Geosystems* 9. <https://doi.org/10.1029/2007GC001699>
- Stein, S., Okal, E.A., 1978. Seismicity and tectonics of the Ninetyeast Ridge area: Evidence for internal deformation of the Indian plate. *J. Geophys. Res. Solid Earth* 83, 2233–2245.

- Stein, C.A., Stein, S., 1992. A model for the global variation in oceanic depth and heat flow with lithospheric age. *Nature* 359, 710–713.
- Stern, R.J., 2002. Subduction zones. *Rev. Geophys.* 40, 1012. <https://doi.org/10.1029/2001RG000108>
- Subrahmanyam, C., Gireesh, R., Chand, S., Raju, K.A.K., Rao, D.G., 2008. Geophysical characteristics of the Ninetyeast Ridge-Andaman island arc/trench convergent zone. *Earth Planet. Sci. Lett.* 266, 29–45. <https://doi.org/10.1016/j.epsl.2007.10.016>
- Tsuboi, S., Kikuchi, M., Yamanaka, Y., Kanao, M., 2000. The March 25,1998 Antarctic Earthquake: Great earthquake caused by postglacial rebound. *Earth, Planets Sp.* 52, 133–136. <https://doi.org/10.1186/BF03351621>
- Turcotte, D.L., Schubert Gerald, 1982. *Geodynamics*, second Edi. ed. Cambridge University Press.
- Wei, S., Helmberger, D., Avouac, J.P., 2013. Modeling the 2012 Wharton basin earthquakes off-Sumatra: Complete lithospheric failure. *J. Geophys. Res. Solid Earth* 118, 3592–3609. <https://doi.org/10.1002/jgrb.50267>
- Weissel, J.K., Enderson, R.N. and Geller, C.A., 1980, Deformation of the Indo-Australian plate, *Nature* 287, 284-291.
- White, R.S., Mckenzie, D. a N., Nions, K.O., 1992. Oceanic Crustal Thickness From Seismic Measurements and Rare Earth Element Inversions. *J. Geophys. Res.* 97, 19,683-19,715.
- Whitney, D.L., Teyssier, C., Rey, P., Roger Buck, W., 2013. Continental and oceanic core complexes. *Bull. Geol. Soc. Am.* 125, 273–298. <https://doi.org/10.1130/B30754.1>
- Whittaker, J.M., Müller, R.D., Sdrolias, M., Heine, C., 2007. Sunda-Java trench kinematics, slab window formation and overriding plate deformation since the Cretaceous. *Earth Planet. Sci. Lett.* 255, 445–457. <https://doi.org/10.1016/j.epsl.2006.12.031>
- Wiens, D.A., DeMets, C., Gordon, R.G., Stein, S., Argus, D., Engdn, J.F., Lundgren, P., Quible, D., Stein, C., Weinstein, S., Woods, D.F., 1985. A diffuse plate boundary model of for Indian Ocean tectonics. *Geophys. Res. Lett* 12, 429–432.
- Yatheesh, V., Dymant, J., Bhattacharya, G.C., Royer, J.Y., Kamesh Raju, K.A., Ramprasad, T., Chaubey, A.K., Patriat, P., Srinivas, K., Choi, Y., 2019. Detailed Structure and Plate Reconstructions of the Central Indian Ocean Between 83.0 and 42.5 Ma (Chronos 34 and 20). *J. Geophys. Res. Solid Earth* 124, 4305–4322. <https://doi.org/10.1029/2018JB016812>
- Yue, H., Lay, T., Koper, K.D., 2012. En échelon and orthogonal fault ruptures of the 11 April 2012 great intraplate earthquakes. *Nature* 490, 245–249. <https://doi.org/10.1038/nature11492>

List of Figures

<p>Figure 1</p>	<p>The diffused plate boundary of Indo-Australian plate identified by Royer and Gordon (1997) marked with purple dashed out lines. The deformation zone is shaded in light pink color. The black arrows indicate the direction of the compression within the deformation zone. The Ninety East Ridge (NER) separates the Fracture zones of Central Indian Basin (CIB) (Yatheesh et al., 2019) and the Wharton Basin (WBH) (Jacob et al., 2014) marked in black solid lines. The dashed black lines represent the reconstructed fracture zones of WBH (Jacob et al., 2014). The South East Indian Ridge (SEIR) is marked in red solid line. The red star denotes the epicenter of the 11th April 2012 Mw 8.6 strike-slip earthquake. The background image represents the free air gravity anomaly derived from satellite altimetry (Sandwell et al., 2014).</p>
<p>Figure 2</p>	<p>Comparison of strike-slip earthquakes extracted from <i>Global Centroid Moment Tensor</i> data base along the ASSZ is performed by categorising the strike-slip focal mechanisms based on their year of occurrence. Focal mechanism for each category is plotted on the background of free air gravity anomaly derived from satellite altimetry (Sandwell et al., 2014). a) represents the distribution of the strike-slip earthquake from 1976 to 26th December 2004 megathrust earthquake which are clustered in three localities mainly the Andaman back arc basin, the south of the Andaman fore arc region and between the southern Sumatran fore arc basin (the Bengkulu basin) and the Java Basin. A prominent clustering of strike-slip earthquakes is evident on the reconstructed Fracture Zones C-D and D-E, close to the Nicobar accretionary island. Inside the Wharton Basin a few strike-slip earthquakes are aligned along the Fracture Zone B-C and C-D and D-</p>

	<p>E b) represents the location of the strike-slip earthquakes spanning between 26th December 2004 and April 11th 2012 earthquakes. The reactivation of the fracture zone is evident by the high magnitude strike-slip earthquakes along the Fracture Zone B-C c) High magnitude strike-slip earthquakes after the 2012 April Wharton basin earthquakes till 2019 are more concentrated along the Fracture Zone B-C representing the continuous reactivation of fracture zones of the Wharton Basin</p>
<p>Figure 3</p>	<p>Free air gravity anomaly derived from satellite altimetry (Sandwell et al., 2014) in the Wharton Basin area. Solid black lines represent actual fracture zones and dashed black lines reconstructed fracture zones. Focal mechanisms extracted from <i>Global Centroid Moment Tensor</i> data base are plotted for earthquakes with magnitude higher than 4.5 Mw and depth less than 60 km for the time span 2004-2019, with colors indicating their year of occurrence. Thick dashed lines on the Ninety East Ridge represents the location of <i>en-echelon</i> faults F1-F1', F2-F2', F3-F3' (after Subrahmanyam et al., 2008).</p>
<p>Figure 4</p>	<p>a) Age of the oceanic lithosphere in the Wharton Basin showing Compartments A to H. Solid black lines represent actual fracture zones and dashed black lines reconstructed fracture zones. Focal mechanisms extracted from <i>Global Centroid Moment Tensor</i> data base are plotted for earthquakes with magnitude higher than 4.5 Mw and depth less than 60 Km for the time span 2004-2019, with colors indicating their depth. Thick dashed lines on the Ninety East Ridge represents the location of <i>en-echelon</i> faults F1-F1', F2-F2', F3-F3' (after Subrahmanyam et al., 2008).</p> <p>b) Three-dimensional view of the subducting lithosphere in the Andaman-Sumatra subduction zone. Solid black lines represent actual fracture zones and dashed black lines reconstructed fracture zones.</p>

	<p>Normally magnetized blocks are displayed in filled colored boxes for the identified isochrons and hollow colored boxes for reconstructed isochrons. Colored circles show the strike-slip earthquake epicenters considered for this study, with colors indicating their depth.</p>
Figure 5	<p>Lithospheric thickness of the Wharton Basin and its reconstructed part. Solid black lines represent actual fracture zones and dashed black lines reconstructed fracture zones. Focal mechanisms extracted from <i>Global Centroid Moment Tensor</i> data base are plotted for earthquakes with magnitude higher than 4.5 Mw and depth less than 60 Km for the time span 2004-2019, with colors indicating their depth. Thick dashed lines on the Ninety East Ridge represents the location of <i>en-echelon</i> faults F1-F1', F2-F2', F3-F3' (after Subrahmanyam et al., 2008).</p>
Figure 6	<p>Bulk lithospheric density of the Wharton Basin and its reconstructed part. Solid black lines represent actual fracture zones and dashed black lines reconstructed fracture zones. Focal mechanisms extracted from <i>Global Centroid Moment Tensor</i> data base are plotted for earthquakes with magnitude higher than 4.5 Mw and depth less than 60 Km for the time span 2004-2019, with colors indicating their depth. Thick dashed lines on the Ninety East Ridge represents the location of <i>en-echelon</i> faults F1-F1', F2-F2', F3-F3' (after Subrahmanyam et al., 2008).</p>
Figure 7	<p>Lithospheric 'subductability' of the Wharton Basin and its reconstructed part. Solid white lines represent actual fracture zones and dashed white lines reconstructed fracture zones. Focal mechanisms extracted from <i>Global Centroid Moment Tensor</i> data base are plotted for earthquakes with magnitude higher than 4.5 Mw and depth less than 60 Km for the time span 2004-2019, with colors indicating their depth. Thick dashed lines on the Ninety East Ridge represents the location of <i>en-echelon</i> faults F1-F1', F2-F2', F3-F3' (after Subrahmanyam et al., 2008).</p>

Figure 8	<p>The satellite bathymetry (GEBCO) of the subducting Northern Wharton basin lithosphere is superimposed by the high-resolution bathymetry (edited version from Graindorge et al., 2008) highlighted in black box. Thick dashed lines on the Ninety East Ridge represents the location of <i>en-echelon</i> faults F1-F1', F2-F2', F3-F3' (after Subrahmanyam et al., 2008). The purple dashed line represents the tear faults T1-T10(Dasgupta et al. 2003; Mukhopadhyay et al. 2009). The solid red line represents the trans-tensional strike-slip faults TF1-Tf4 (Mukhopadhyay et al. 2016) Details of the fracture zones and focal mechanisms are same as Figure 5,6 and 7.</p>
Figure 9	<p>Schematic representation of the stress buildup due to the subductability contrast along the Fracture Zone B-C. The solid black line represents the current position of the subducting lithosphere and the dashed black line represents the subducting slab after the tearing. Due to the differential slab pull by the thicker/denser lithosphere of Compartment B and thinner/lighter lithosphere of the Compartment C, the stress along the Fracture Zone B-C increases causing strike-slip earthquakes. Eventually with the advancement of subduction, the increasing slab pull will lead to the tearing of the lithosphere along the prevalent fracture zone providing the provision to release the accumulated stress and prevent further stress buildup.</p>
Figure 10	<p>Depth contours imaged by Pesicek et al., 2008; 2010 is superimposed on a) free air gravity anomaly derived from satellite altimetry (Sandwell et al., 2014) b) age grid of the Wharton lithosphere. The red dashed lines BC', CD' and DE' represents the actual location of the transform faults associated with the Andaman Sea spreading. IFZ', H1', H2' and H3' marks the hinges of the folds on the depth contours of the subducting slab</p>

Figure 11	<p>The schematic representation of the subducting northern Wharton lithosphere at the Sunda Trench. The subductability contrast between each lithospheric compartment is represented in different color code; purple-High, light green- medium, light blue-low, yellow-lowest. Black dots represent the strike-slip earthquakes along the Fracture Zone B-C due to the high subductability contrast between the fracture zone Compartments B and C. Though a similar high subductability contrast is observed between the Compartment G and H, the vertical tearing along the IFZ (Chesner, 1998, 2012) prevents the stress accumulation and associated seismicity. The horizontal tear (Richards et al. 2007; Singh and Moeremans, 2020) formed by the slab break off due to the excess slab pull at the older edges of Compartment C and D might have initiated the spreading in the Andaman Sea. The horizontal tear proposed in the Compartment E-F corresponds to the tearing under the Burma plate (Pesicek et al., 2008; 2010).</p>
-----------	--

List of Table

Table 1	<p>Thickness, bulk-density and subductability estimated for the subducting northern Wharton lithosphere at the Sunda trench. Age of the magnetic chrons according to the GeomagneticPolarity Timescales of Cande and Kent (1995). The letters 'y' and 'o' are acronyms for 'younger' and 'older' chron respectively.</p>
---------	--